



Creasy, N., Pisconti, A., Long, M. D., Thomas, C., & Wookey, J. (2019). Constraining lowermost mantle anisotropy with body waves: A synthetic modeling study. *Geophysical Journal International*, 217(2), 766-783. <https://doi.org/10.1093/gji/ggz049>

Peer reviewed version

Link to published version (if available):
[10.1093/gji/ggz049](https://doi.org/10.1093/gji/ggz049)

[Link to publication record in Explore Bristol Research](#)
PDF-document

This is the author accepted manuscript (AAM). The final published version (version of record) is available online via Oxford University Press at <https://academic.oup.com/gji/article/217/2/766/5303728>. Please refer to any applicable terms of use of the publisher.

University of Bristol - Explore Bristol Research

General rights

This document is made available in accordance with publisher policies. Please cite only the published version using the reference above. Full terms of use are available:
<http://www.bristol.ac.uk/red/research-policy/pure/user-guides/ebr-terms/>

1
2
3 **Constraining lowermost mantle anisotropy with body waves: A synthetic modeling**
4 **study**

5
6 Neala Creasy^{1*}, Angelo Pisconti², Maureen D. Long¹, Christine Thomas², and
7 James Wookey³
8

9 ¹Department of Geology and Geophysics, Yale University

10 ²Institut für Geophysik, Universität Münster

11 ³Department of Earth Sciences, University of Bristol

12 *Corresponding author. Email: neala.creasy@yale.edu
13
14

Summary

Different mechanisms have been proposed as explanations for seismic anisotropy at the base of the mantle, including crystallographic preferred orientation of various minerals (bridgmanite, post-perovskite, and ferropericlasite) and shape preferred orientation of elastically distinct materials such as partial melt. Investigations of the mechanism for D" anisotropy usually yield ambiguous results, as seismic observations rarely (if ever) uniquely constrain a mechanism or orientation and usually rely on significant assumptions to infer flow patterns in the deep mantle. Observations of shear wave splitting and polarities of SdS and PdP reflections off the D" discontinuity are among our best tools for probing D" anisotropy; however, currently available datasets cannot constrain one unique scenario among those suggested by the mineral physics literature. In this work, we determine via a forward modeling approach what combinations of body wave phases (e.g. SKS, SKKS, and ScS) are required to uniquely constrain a mechanism for D" anisotropy. We test nine models based on single-crystal and polycrystalline elastic tensors provided by mineral physics studies. Our modeling predicts fast shear wave splitting directions for SKS, SKKS, and ScS phases, as well as polarities of P and S wave reflections off the D" interface, for a range of propagation directions, via solution of the Christoffel equation. We run tests using randomly selected synthetic datasets based on a given starting model, controlling the total number of measurements, the azimuthal distribution, and the type of seismic phases. For each synthetic dataset, we search over all possible elastic tensors and orientations to determine which are consistent with the synthetic data. Overall, we find it difficult to uniquely constrain the mechanism for anisotropy with a typical number of seismic anisotropy measurements (based on currently available studies) with only one measurement technique (SKS, SKKS, ScS, or reflection polarities). However, datasets that

39 include SKS, SKKS, and ScS measurements, or a combination of shear wave splitting and
40 reflection polarity measurements, increase the probability of uniquely constraining the
41 starting model and its orientation. Based on these findings, we identify specific regions
42 (i.e., North America, northwestern Pacific, and Australia) of the lowermost mantle with
43 sufficient raypath coverage for a combination of measurement techniques.

44 Abbreviated Title: Constraining lowermost mantle anisotropy

45

46 Keywords (up to 6):

- 47 • Seismic anisotropy
- 48 • Composition and structure of the mantle
- 49 • Mantle processes
- 50 • Statistical seismology

1. Introduction

Mantle convection finds its surface expression in plate tectonics and represents a crucial dynamic process in the deep Earth. Despite its importance, the pattern of mantle convection and the forces that drive mantle flow remain imperfectly understood. This is particularly true for the deepest mantle: flow at the base of the mantle likely influences (and/or is influenced by) structures such as large low shear velocity provinces (LLSVPs). Subducting slabs likely penetrate into the lower mantle and hot mantle plumes generate from or near the LLSVPs, indicating a strong connection between the surface and deep mantle processes (e.g., Garnero et al., 2016).

Observations of seismic anisotropy have the potential to illuminate mantle flow, due to the relationship between strain due to mantle convection and seismic anisotropy via lattice preferred orientation (LPO) or shape preferred orientation (SPO) mechanisms. The presence of anisotropy in the D" layer at the base of the mantle has been known for several decades (e.g., Lay and Helmberger, 1983) from the analysis of body wave phases (as summarized in Nowacki et al., 2011). At this point a relatively small fraction (Figure 1) of the core mantle boundary region has been explored for D" anisotropy using body waves. Figure 1 shows a map, updated from Nowacki et al. (2011) illustrating the geographical coverage of previous studies (including recent work by Creasy et al., 2017, Deng et al., 2017, Simmons et al., 2015, Ford et al., 2015, Long and Lynner, 2015, Lynner and Long, 2014, Cottaar and Romanowicz, 2013, and Thomas et al., 2011). Despite these observations, however, we still do not fully understand the anisotropy in these regions. Several different models for D" anisotropy have been proposed, including those that invoke LPO of bridgmanite (Br), post-perovskite (Ppv), or ferropericlase (Fp), and those that invoke SPO of partial melt (see Nowacki et al., 2011 for a review). The mechanisms

75 responsible for D" anisotropy, the dominant slip systems involved, the orientation of the
76 anisotropic fabric, and the implications for mantle flow geometries thus remain poorly
77 understood.

78 A variety of body waves has been used to study anisotropy in the deepest mantle.
79 Specifically, direct S, ScS, and Sdiff have been used to observe lowermost mantle
80 anisotropy by measuring shear wave splitting (e.g., Wookey et al., 2005a, Cottaar and
81 Romanowicz, 2013, Thomas et al., 2007, Ford et al., 2006). Combinations of phases, such
82 as SKS-SKKS (e.g., Wang and Wen, 2007; Long, 2009) or S-ScS (e.g., Wookey et al.,
83 2005a; Nowacki et al., 2010), are often useful to isolate the lowermost mantle contribution
84 to splitting. Thomas et al. (2011) used an array analysis technique to observe reflected P
85 and S waves off the D" discontinuity; the azimuthal dependence of the polarity of D"
86 reflections SdS and PdP contains information about lowermost mantle anisotropy. While
87 body wave observations have been extensively used to study anisotropy at the base of the
88 mantle, such studies suffer from the fundamental limitation of small azimuthal coverage;
89 most studies are essentially restricted to a single raypath, which means that the geometry
90 of anisotropy cannot be tightly constrained.

91 Several recent studies of deep mantle anisotropy have ameliorated this limitation
92 by targeting regions of D" that are sampled by body waves over multiple azimuths (pink
93 regions in Figure 1). These include studies of the lowermost mantle beneath Siberia
94 (Wookey and Kendall, 2008; Thomas et al., 2011), North America (Nowacki et al., 2010),
95 the Afar region of Africa (Ford et al., 2015), and Australia and New Zealand (Creasy et al.,
96 2017). In some cases, one can test whether the observations could clearly distinguish
97 among different mechanisms for anisotropy. For example, Ford et al. (2015) and Creasy et
98 al. (2017) carried out forward modeling of ScS, SKS, and SKKS splitting datasets over

multiple azimuths to test whether a unique mechanism for anisotropy and/or a unique orientation of an assumed mechanism could be identified. In each of these studies it was found that LPO of Ppv matches the observations, but other mechanisms (such as LPO of Br or Fp) were also consistent with the data. None of the studies summarized in Figure 1 has successfully identified a uniquely constrained mechanism or orientation for anisotropy. Motivated by this, we attempt here to understand what observations are needed to distinguish the various possible models for D'' anisotropy.

The goal of this study is to understand what combination of body wave datasets (SKS, SKKS, ScS, and reflection polarities) are necessary to uniquely constrain the mechanism and geometry of anisotropy in the lowermost mantle using observations of shear wave splitting and D'' reflection polarities. Such an understanding will aid in the design of future observational studies to maximize the chances of uniquely constraining a mechanism. We are interested in understanding the characteristics of datasets that are best suited to constrain the details of D'' anisotropy, including the number of measurements needed, the optimal azimuthal coverage, and the optimal combinations of body wave phases. We address two specific questions: 1) What types of datasets (potentially including SKS, SKKS, and/or ScS splitting, and/or reflection polarities) are needed to uniquely identify the causative mechanism for anisotropy (e.g., LPO of Ppv, Br, Fp, or SPO of partial melt)? and 2) if we assume that the mechanism for anisotropy is known to be LPO of Ppv, what type of datasets are needed to uniquely constrain the orientation of the anisotropy?

We carry out forward modeling tests for a suite of synthetic body wave data. Our approach to forward modeling of synthetic datasets follows our previous work on observations of shear wave splitting in D'' (Ford et al., 2015; Creasy et al., 2017) and also incorporates measurements of D'' polarities of P and S wave reflections (Thomas et al.,

2011a). Our approach is to test a variety of candidate elastic tensors that describe various mechanisms for lowermost mantle anisotropy. For each model, we randomly generate more than 5,000 unique synthetic datasets (for SKS, SKKS, and ScS shear wave splitting, plus PdP and SdS polarities) with a certain set of characteristics (e.g., number and type of measurements, as described below) and a random azimuthal distribution. For each set of random raypaths, we compute a set of predicted “observations” of shear wave splitting and/or reflection polarities using a ray theoretical approach. We then attempt to determine what characteristics of body wave datasets are optimal for uniquely constraining anisotropy in the lowermost mantle.

2. Methods

2.1 Candidate models for D” anisotropy

We first consider which plausible models for D” anisotropy should be tested. The lower mantle is likely composed of pyrolite (e.g., Lee et al., 2004), a model composition that consists of ~76 mol% of bridgmanite (Br: MgSiO_3), ~17 mol% of periclase (Fp: $(\text{Mg,Fe})\text{O}$), and ~7 mol% of calcium perovskite (Capv: CaSiO_3). In the D" layer at the base of the mantle, we expect a phase change of Br to post-perovskite (Ppv: MgSiO_3) (e.g., Murakami et al., 2004). Based on *ab initio* calculations and laboratory experiments, Br, Fp, and Ppv all have strong single-crystal anisotropy, with Fp being the weakest mineral and the most anisotropic (as summarized in Nowacki et al., 2011), although it is less abundant than Br/Ppv. This suggests that LPO development in any of the dominant lowermost mantle minerals may contribute to the observed anisotropy, as long as deformation is taking place in the dislocation creep regime (e.g., McNamara et al., 2001). Another possible mechanism is aligned pockets of an elastically distinct material such as partial melt in configurations

such as disks, tubes, or sheets, creating shape preferred orientation (SPO) (e.g., Kendall and Silver, 1998) (Tables 1 and 2).

We test a suite of models that describe single-crystal elasticity of lowermost mantle materials derived from *ab initio* calculations, following our previous modeling work (Ford et al., 2015; Creasy et al., 2017). This approach assumes that an aggregate will have the same anisotropic geometry (although not strength) as a single crystal. In addition to the single-crystal models, we test one model (for Fp LPO) based on deformation experiments (Long et al., 2006) and models that invoke the SPO (shape-preferred orientation) of partial melt (Table 1), with elastic constants calculated using an implementation of effective medium theory within the MSAT toolbox (Walker and Wookey, 2012).

Finally, our last candidate model approximates a textured Ppv aggregate and is derived from a 3D, global mantle flow field calculation in combination with a visco-plastic self-consistent model LPO development in Ppv (Walker et al., 2011). We determined a representative elastic tensor for Ppv texture development in high-strain simple shear by querying the TX2008.V1.P010 model of Walker et al. (2011), which combined a lower mantle viscosity model from Mitrovica and Forte (2004) with a mantle density model from Simmons et al. (2009). We only considered the case in which slip on the (010) plane dominates; this is the most likely slip plane for Ppv based on experiments (Walte et al., 2009; Yamazaki et al., 2006), modeling (Goryaeva et al., 2017), and observations of D'' anisotropy (Creasy et al., 2017; Ford et al., 2015; Thomas et al., 2011). To obtain a representative average tensor for simple shear, we identified a 15° by 15° geographical region of the global flow (beneath the northern Atlantic Ocean) that is dominated by strong horizontal shear. We then extracted the 16 elastic tensors (the model calculated tensors

every 5°) from the resulting TX2008.V1.P010 elasticity predictions in this region averaged them.

2.2 Computation of reflection polarities and fast splitting directions

Given the full suite of candidate models for elasticity in D'' to be used in our study (Table 1), we implement methods for predicting various types of body wave observations for these scenarios. We calculated predicted shear wave splitting fast directions for SKS, SKKS, and ScS phases (Figure 2) over a range of azimuths (every 5°) and inclinations for each of these models (Tables 1) by solving the Christoffel equation using the MSAT toolkit of Walker and Wookey (2012). The three different phases propagate at different inclination angles: ~55°, 35°, 0° from the horizontal, respectively.

We then calculated the reflection polarities of SdS and PdP and the corresponding predicted shear wave splitting fast directions (Figure 3) over a range of azimuths (every 5°) and inclinations for each of these models (Tables 1 and 2). Table 2 summarizes the models used to generate predictions of D'' reflection polarities (SdS and PdP), including the assumed slip system, based on the methodology of Thomas et al. (2011). These models were constructed by assuming horizontal simple shear at the base of the mantle, where the dominant slip direction aligns parallel to the CMB, the slip plane is assumed to be horizontal, and 12% of the aligned single crystals are mixed linearly with its isotropic equivalent. This choice of 12% alignment was based on the previous work of Thomas et al. (2011), and yields reasonable anisotropic strengths; since we focus on reflection polarities and not amplitudes, however, this choice of value is not critical. We assume that the aligned grains are sub-parallel with the slip direction and the slip plane is sub-parallel to the CMB and the remaining grains are randomly oriented for Models A, B, and C (Figure

3). We tested three models (Models A [Ppv], C [Br], and D [Fp] in Table 2) in which the D'' discontinuity represents a change in alignment of the mineral grains from an isotropic (above the discontinuity) to an anisotropic (below the discontinuity) regime. In Model B, the D'' discontinuity is an isotropic phase transformation from Br to anisotropic Ppv. The predicted values for reflection polarities for each model are shown in Figure 3 and were calculated using Guest and Kendall (1993) from the velocity perturbation and reflection coefficients at the interface between an isotropic and anisotropic layer with respect to azimuth from the dominant slip direction and epicentral distance (Thomas et al., 2011).

Our approach to calculating predicted shear wave splitting parameters and reflection polarities for our synthetic models makes several simplifying assumptions. First, we only directly model shear wave splitting due to lowermost mantle anisotropy, and ignore any potential contributions from the upper mantle. Our approach therefore assumes that any upper mantle contribution (in real data) has been correctly accounted for; we further assume that the bulk of the lower mantle is isotropic (Meade et al., 1995). We do not explicitly consider how incorrect upper mantle corrections could bias the resulting D'' observations, which is beyond the scope of our study. Second, we rely on ray theory and do not consider finite frequency wave effects in our modeling. Ray theoretical predictions are generally adequate for homogenous regions of D'' (e.g., Nowacki and Wookey, 2016), although they may break down for laterally heterogeneous anisotropic models (heterogeneities varying over hundreds of km). Third, in our modeling we approximate the propagation directions for SKS and SKKS with average inclination angles for these phases, and for ScS we assume that propagation is horizontal through the D'' layer. This assumption follows previous work (Nowacki et al., 2010; Ford et al., 2015; Creasy et al., 2017). In the Earth and at the relevant epicentral distances, ScS can be inclined from the horizontal up

to $\sim 15^\circ$, but this assumption has only a modest effect on the predicted splitting parameters. We assume the three different phases (SKS, SKKS, and ScS) propagate at different inclination angles: $\sim 55^\circ$, 35° , 0° from the horizontal, respectively. Inclination angles are based on a straight-line approximation, calculated using TauP (Crotwell et al., 1999) based on the PREM Earth model (Dziewonski and Anderson, 1980) for distances of $90^\circ - 120^\circ$ for SKS/SKKS and $60^\circ - 80^\circ$ for ScS with an event at a depth 10 km. We use these average propagation angles for SKS and SKKS in our modeling for simplicity, although for real data they can vary by up to $10^\circ - 20^\circ$ from these average values.

2.3 Modeling approach and strategy

Our goal is to conduct a series of stochastic forward modeling simulations to test whether we can uniquely constrain a given starting model (an elastic tensor) and its orientation using a dataset with a given set of characteristics (e.g., number and type of measurements, azimuthal distribution). Our forward modeling framework follows Ford et al. (2015), who modeled a shear wave splitting dataset that samples the lowermost mantle beneath the Afar peninsula along the edge of the African LLSVP. We did not consider delay times in our modeling. Individual delay time measurements contain larger error bars, which limit the utility of using the relative travel times in a dataset as a discriminant. The complete tradeoff between fabric strength and layer thickness also limits the utility of using absolute travel times as a constraint.

For each of our modeling experiments, we first choose a starting model and orientation from the possibilities listed in Table 1. As an example, we first consider a horizontally aligned elastic tensor of Ppv with $[100]$ and $[010]$ axes parallel to the CMB, which we will use to illustrate our approach in several of the following figures. Second, we

randomly identify a set of raypaths of SKS, SKKS, and/or ScS sometimes in combination with SdS and PdP reflection polarities. Third, we calculate the predicted fast-axis directions and/or reflection polarities of SdS and PdP for each raypath, as described in Section 2.2.

In the fourth step, we model the synthetic dataset by applying the same forward modeling technique that we typically use for real data (Ford et al., 2015). Specifically, we treat the synthetic observations as though the actual model used to generate them was not known, and test all possible models listed in Tables 1 and 2) in all possible orientations (every 5°) to identify models/orientations that are consistent with the synthetic dataset. A candidate model/orientation is discarded if the predicted and “observed” fast splitting directions differ by more than 20° or if the predicted reflection polarities are opposite those of the “observations”. We apply this 20° cutoff for the splitting observations, based on methods and reasonable estimates of errors in previous shear wave splitting studies (see Ford et al., 2015). While this misfit criterion is appropriate for measurement errors, it does not take into account effects such as inaccurate upper mantle corrections for actual D” anisotropy observations, or the possible finite-frequency effects of complex structure. Explicit consideration of these effects in D” anisotropy studies is a subject of ongoing research. For each candidate model/orientation that was considered an acceptable fit to the synthetic data, we calculated a total misfit value (for the fast polarization directions only) based on a residual sum of squares approach, following Ford et al. (2015). Each fast direction misfit is normalized by the maximum residual of 90° and summed by using the residual sum of squares, in which we calculate the square of the difference between the observation and data prediction.

The fifth and final step in our modeling strategy is to repeat the entire process a large number (M) of times for random raypath configurations. All of these steps are

illustrated in Figure 4. In each iteration, we randomly choose a new azimuthal distribution of raypaths for a new synthetic dataset with varying characteristics (such as the number and type of observations, described in more detail below). We report our results by considering what percentage of the M iterations could uniquely identify the starting model. Each individual iteration was designated as “*uniquely constrained*” if it successfully identified the correct starting model, and could completely rule out any other candidate model. However, if there was at least one other anisotropy configuration (any candidate elastic tensor model, in any orientation) was found to be consistent with the synthetic observations, that iteration was designated “*not uniquely constrained*.” Therefore, all our model results are characterized through a %-*uniquely constrained* value, which identifies how what percentage of the M simulations could uniquely constrain the starting model. The actual values of these “%-uniquely constrained” estimates are strongly dependent on our modeling choices, and the estimates could change with different modeling assumptions. However, these percentages can be compared across our suite of numerical simulations, since our assumptions are consistent across the various tests.

Within this modeling framework, we tested a series of synthetic dataset characteristics described the following three distinct variables: the number of measurements (N), ratio of the number of SK(K)S (that is, SKS plus SKKS) measurements to the total number of shear wave splitting measurements (we term this ratio the “SKS number”), and the azimuthal distribution of measurements, as quantified by the angular dispersion (R). Angular dispersion is defined as:

$$C_P = \sum_{i=1}^n \cos(a_i), \quad S_P = \sum_{i=1}^n \sin(a_i), \quad (1)$$

$$R = \sqrt{C_P^2 + S_P^2}, \quad (2)$$

where α_i is a vector of directions and R is angular dispersion, which varies from 0 (uniform dispersion) to 1 (concentration in one direction) (Mardia and Jupp, 2000). A graphical definition of R is shown in Supplementary Figure S1.

We tested different combinations of N and SKS number to gain insight into how many measurements, and in what combination, are typically needed to uniquely constrain the anisotropy. For angular dispersion, we calculated the value of R for each of the M iterations carried out in each test; then, we queried the large number of simulations to understand how the azimuthal distribution of the synthetic data affected its ability to constrain anisotropy.

2.4 Distinguishing the mechanism and orientation of anisotropy

For the first round of tests, we sought to understand how many shear wave splitting measurements, and in what combination (as described by the SKS number), are generally needed to uniquely constrain the *mechanism* for anisotropy. That is, we tested whether synthetic datasets could be shown to be consistent *only* with the correct starting model (e.g., Ppv, as opposed to other models listed in Table 1), and with *no other* candidate mechanism. For this round of tests, we used the single crystal models in Table 1 as starting models, each in several different orientations. The LPO model of Ppv was only used for the second round of tests. We defined the starting model orientation via the rotation angle about the [100] axis from the horizontal (note that Figure 2 only shows an example with a horizontal [100] and [010] direction). We arbitrarily tested each single crystal model at three different orientations based on the rotation angle about the [100] axis from the horizontal: 0°, 45°, and 90°. For the LPO model of Ppv, we only test the original orientation for the starting model and do not test a rotated version of the elastic tensor since this model is based on a

region in the Walker et al. (2011) with horizontal shear. In our initial round of tests, we focused only on cases in which shear wave splitting observations of SKS, SKKS, and ScS (for varying N, SKS number, and R values) were used to constrain the models; in later tests, we explored scenarios in which reflection measurements were combined with shear wave splitting data, in order to estimate the improvement obtained by combining different data types.

We also carried out a series of tests whose goal was to constrain the *orientation* of the elastic tensor for the case in which the mechanism for anisotropy is known (or assumed). For this line of inquiry, we focused on Ppv as a test case; we did not test other mechanisms in this part of the study. The choice to focus on Ppv was made for simplicity and because Ppv is often invoked as the preferred mechanisms for anisotropy in D" (Creasy et al., 2017; Ford et al., 2015; Ford and Long, 2015; Nowacki et al., 2010; Thomas et al., 2011a; Wookey et al., 2005b). We consider both single-crystal Ppv tensors and elastic tensors derived from texture modeling, as discussed above. As in our first series of tests, we initially focus on synthetic datasets that only contain shear wave splitting observations, and then examine cases that also include reflection measurements.

Lastly, in addition to the two major lines of inquiry we address in our modeling (what kind of datasets are needed to constrain the *mechanism* and *orientation*) of lowermost mantle anisotropy, we performed two practical tests using horizontal Ppv as a starting model. First, we carried out a test of how many iterations (that is, values of M) are needed for our forward algorithm to converge on an estimate of the probability of identifying unique models. Second, we tested the addition of Gaussian noise to the shear wave splitting predictions, in order to understand how well real, noisy datasets might perform. The results of these practical tests are described below. While seismic data can deviate from a Gaussian

distribution (Groos and Ritter, 2009), we only consider Gaussian distributed noise here since in an ideal case, seismic noise is Gaussian distributed (Bendat and Piersol, 2011).

3. Results

3.1 Illustrative examples: Model runs for a ppv starting model

To illustrate the process and results of our modeling, we discuss here the results from a test that attempts to constrain the *starting model*, as well as one iteration of a test that attempts to constrain the *orientation*. In both cases, we use synthetic shear wave splitting data only. For these examples, as in all of our tests, we follow the five steps of our method outlined above (Figure 4): (1) choose a starting model and orientation, (2) choose the number of observations and the SKS number to randomly generate a distribution of raypaths, (3) calculate the predicted fast polarization directions (of SKS, SKKS, and ScS) and reflection polarities (for SdS and PdP) for the synthetic dataset for the chosen starting model, (4) conduct a forward modeling search over all possible orientations for all possible candidate models to eliminate all models/orientations that do not fit the “observations” using a misfit cutoff. Then, if all other models and orientations can be eliminated by applying the misfit cutoff, this set of synthetic raypaths are able to uniquely constrain the starting model and designated as “*uniquely constrained*.” The fifth step would be repeating this process M number of times but for this illustrative example, $M = 1$.

Our illustrative example is shown in Figure 5. For this example, we chose a starting model of non-rotated Ppv (in this case, the [100] and [010] crystallographic axes are parallel to the CMB) (Figure 5a). In all of our single-crystal elasticity tests, we do not assume a dominant slip system; rather, we invoke a starting orientation in the geographic reference frame identified by the angle of the mineralogical axes. This particular example

involves 9 splitting observations, 6 of which are SK(K)S (that is, an SKS number of 2/3). The randomly generated azimuthal distribution of these chosen phases is shown in Figure 5b. The predicted fast polarization directions for our chosen model and ray configuration, plotted in a ray-centered reference frame, are shown in Figure 5c. A search over all possible candidate models and orientations (rotating every 5°) shows that there is no other model, other than the correct starting model (Ppv), that can match each of the synthetic fast splitting directions to within 20° (our pre-defined misfit cutoff). Put another way, for every possible combination of starting model and orientation (other than the correct, known starting model), at least one predicted fast splitting orientation differed from that in the dataset by more than the 20° misfit cutoff. Since this particular configuration of observations could uniquely identify the starting model and no other models, it is designated “*uniquely constrained*.”

This particular example illustrates a single iteration ($M = 1$) of our testing, but the power of our approach lies in repeating this a large number of times to understand what percentage of randomly generated synthetic datasets have the ability to uniquely constrain the starting model. In order to understand how many iterations are needed to converge on an estimate of this probability, we conducted an “iteration test” for our horizontal Ppv starting model, as shown in Figure 6. For this test, we used 9 shear wave splitting measurements ($N = 9$) and an SKS number of 2/3, as in the example shown in Figure 5, and ran a large number of iterations ($M = 50,000$), each involving a new, random distribution of propagation azimuths. After each successive iteration, we calculated the percentage (of M iterations) for which the synthetic dataset was able to *uniquely constrain* the starting model, as shown in Figure 6. For this starting model, after a large number of iterations, we found that 41% of all iterations could uniquely constrain the starting model,

while for the other 59% of the raypath configurations, there was another model/orientation that could simulate the synthetic data. Our running estimate of how likely a dataset with 9 splitting observations (6 SK(K)S, 3 ScS) converges on an average value of 41% after approximately 1,000 iterations (Figure 5). Based on this iteration test, we have chosen to run each of our numerical experiments for $M = 5,000$ iterations, balancing computational cost and the need for our estimates to converge.

Next, to illustrate our process for testing whether synthetic data can identify a unique starting *orientation*, we show in Figure 6 two examples of searching for the correct starting orientation for the same horizontal Ppv starting model as in Figure 4. For this example, we chose two different raypath configurations, one with $N = 8$ observations (5 SKS+SKKS and 3 ScS; Figure 7a) and one with $N = 4$ (3 SKS+SKKS and 1 ScS; Figure 7b). We assume that the mechanism for anisotropy is known to be Ppv and that the elastic constants are known, and search over all possible orientations to test whether there are additional configurations (other than the known starting orientation) that can reproduce the synthetic observations.

Figures 7a and 7b show all possible orientations that satisfy this suitability criterion for each of our two examples ($N = 8$ and $N = 4$, respectively), with each orientation color-coded by its calculated misfit value (Equation 1). Following Ford et al. (2015), we search for local minima of misfit within the 3-D rotation space. For our $N = 8$ case (Figure 7a), the set of 8 measurements could uniquely identify the starting orientation, and would be designated as “uniquely constrained.” However, for our $N = 4$ case (Figure 7b), we identified two other possible orientations (that is, the known correct starting orientation, plus two others). Therefore, for this particular raypath configuration, the solution is

designated “not uniquely constrained.” We note, however, that the orientation with the lowest misfit value (magenta dot in Figure 7b) is, in fact, the correct starting orientation.

Finally, we illustrate an example calculation that includes Gaussian noise in the synthetic observations (Figure 7c). This test relies on the same horizontal Ppv starting model, and uses the same raypath configuration ($N = 4$) as the test shown in Figure 7b. The only difference is that when the predicted shear wave splitting fast directions are calculated based on the starting model and raypath distribution, we add Gaussian noise to the fast splitting direction “observations,” with a maximum error excursion of 20° and a standard deviation of 9° . Figure 7c reveals that the case with Gaussian noise produced the same two possible sets orientations as fitting the data, but now the solution with the minimum misfit is not associated with the correct solution.

3.2 Results: Constraining the anisotropy mechanism

Building on the illustrative examples discussed in section 3.1, we now explore the results of a large number of simulations with different starting models and raypath configurations. We first address the question of what kind of datasets are needed to distinguish among the various models listed in Figures 2 and 3. For this suite of numerical experiments, we examined a variety of starting models and orientations, as well as a variety of raypath configurations (as defined by the number of splitting measurements, the SKS number, and the angular dispersion of the raypath azimuths). The results of these experiments are shown in Figure 8. We first examine those model runs that only included shear wave splitting data, shown in the nine panels of Figure 8a.

We initially focus on the mechanism and orientation of the starting model (Figure 8a, left panels), and explore how the probability of uniquely constraining the mechanism

varies as a function of the number of measurements. For each of the models considered, the probability of identifying the unique starting model increases with the number of measurements, as expected, typically with a sharp increase in the probability for N values between ~ 6 -9. In all cases, approximately 9 measurements are needed in order to have a $\sim 50\%$ chance of constraining the starting model, while a high number of splitting measurements ($N \approx 15$) is needed for the probability to reach $\sim 90\%$. (For comparison, the datasets of Ford et al. (2015) and Creasy et al. (2017) contained between 4-8 splitting measurements.) The starting model with the highest success rate at constraining the mechanism is Br, as opposed to Fp and Ppv.

The probability of constraining the starting mechanism depends on the orientation of the starting model; as shown in Figure 8a, we tested orientations with a horizontal [100] crystallographic axis, 45° rotated about the [100], and 90° rotated about the [100] axis. Interestingly, for Ppv it is easier to uniquely constrain the starting model in the 90° case; in contrast, for Br the chances are highest for the horizontal case, and for Fp the chances are substantially higher for the tilted case. The reason for this result for Ppv can be discerned by examining the predicted splitting patterns in Figure 2. For the horizontal case, predicted fast splitting directions for ScS do not vary with azimuth; however, if the Ppv tensor is rotated by 90° about the [100] axis, there is significant variation in fast directions with azimuth. With greater variability in the predicted fast polarization directions (lower angular dispersion), there is a higher probability of constraining that model for a given number of ScS observations. A similar principle is at work for Fp: ScS fast directions do not vary with azimuth for either horizontally or vertically aligned Fp, but in the tilted case, variability is present. Generally, the anisotropy scenarios that yield higher chances of uniquely constraining the starting model have lower mean angular dispersion values of the

456 predicted fast-axis directions (Supplementary Figure S2). Models that have little variation
457 in fast-axis directions with azimuth, such as non-rotated Fp, are more difficult to uniquely
458 constrain (Figure S2c and Figure 8a).

459 We also examined how the balance between SKS+SKKS vs. ScS phases in the
460 synthetic dataset affected the ability of the synthetic “observations” to uniquely constrain
461 the starting model (Figure 8a, middle panels). For these experiments, we varied the SKS
462 number from 0 (all ScS measurements) to 1 (all SKS+SKKS measurements) for a fixed
463 value of $N = 9$. For very high or low values of SKS number we find a low probability of
464 uniquely constraining the starting model with substantially higher probabilities for
465 intermediate SKS numbers. The optimal ratio of SK(K)S phases to total measurements
466 differs slightly for different starting models, but in general an SKS number between 0.5
467 and 0.8 maximizes the chances of constraining the anisotropic mechanism. In all cases, a
468 combination of ScS and SK(K)S shear wave splitting observations, instead of splitting
469 measurements for just one phase type, will drastically improve the probability of
470 constraining the starting model.

471 Additionally, we explored the importance of how the angular distribution of the
472 synthetic raypaths affected the ability to constrain the starting model, finding only a weak
473 effect (Figure 8a, right panels). As expected, datasets with a wide angular distribution (R
474 < 0.2) have the largest probability of uniquely constraining the starting model in all cases.
475 At very large values of angular dispersion ($R > 0.8$), for which the raypaths are clustered
476 over a narrow range of azimuths, the splitting “observations” are sampling similar parts of
477 the elastic tensor. Because of this, datasets that are tightly clustered in azimuth cannot
478 capture the symmetry of the tensor and cannot distinguish among different candidate

mechanisms for anisotropy. For intermediate values of R , the dependence on R is not strong.

Finally, we explored the value of combining shear wave splitting and reflection polarity measurements when trying to uniquely constrain an anisotropic model. Figure 8b shows the results of adding a single reflection polarity measurement (that is, a measurement of PdP and SdS polarities for a single raypath) to a dataset of shear wave splitting measurements. For this test, we considered a smaller number (four) of potential candidate models (as shown in Figure 3), so the probabilities of uniquely constraining the anisotropy mechanism are generally higher than in our other tests. For this test, we chose a raypath configuration involving an SKS number of 0.67 and varied the number of shear wave splitting measurements from 0 to 15. We used a starting model A in Figure 3 (anisotropy due to Ppv), and tested configurations that involved both shear wave splitting measurements and one additional set of reflection polarity measurements (both PdP and SdS) at a single azimuth. This test (Figure 8b) demonstrates that despite the fact that reflectivity measurements provide only binary information (positive or negative polarities), the incorporation of a different data type into the test increases the probability of uniquely constraining the starting model. In some cases, this increase is substantial; specifically, for datasets containing between 4 and 8 shear wave splitting measurements. The addition of reflection polarity data can increase the probability of constraining the starting model by ~10-18% (right panel of Figure 8b).

3.3 Results: Constraining the anisotropy orientation

The tests shown in Figure 8 illustrate the ability of shear wave splitting and reflection polarity data to constrain the anisotropic mechanism if the algorithm is allowed

to consider a range of possible models. We now turn our attention to tests in which we assume that the mechanism that creates the anisotropy, as well as the elastic constants associated with that mechanism, are known, but the orientation of the elastic tensor is not known. In general, this is an easier problem than uniquely constraining the starting model, as the observations need not distinguish among different candidate elastic tensors, only among different possible orientations. In practical terms, this type of modeling exercise would be suitable for datasets that sample a region of the lowermost mantle whose mineralogy and temperature conditions can be constrained using independent observations or models (for example, seismic velocities in combination with mineral physics constraints).

For this set of tests, we first consider single-crystal Ppv in three different configurations: 1) [100] and [010] axes oriented in the horizontal plane, 2) a 90° rotation about the [100] axis, and 3) randomly chosen orientations. For the third configuration, we randomly identified nine different, unique starting orientations. These randomly generated orientations were used for each of the ~5,000 iterations in this scenario. As with the tests discussed in section 3.2, we tested a variety of raypath configurations with a range of N (number of measurements), SKS number, and examined how our results varied with the angular dispersion characteristics of the synthetic raypaths. The results of our single-crystal Ppv tests are shown in the top row of Figure 9. The results for our collection of nine random starting orientations are shown in detail in Supplementary Figure S3.

As expected, our tests demonstrate that uniquely constraining the orientation of the starting model is much easier and requires fewer measurements than uniquely constraining the starting model/mechanism (Figure 7). In general, a ~50% probability of correctly retrieving the anisotropy is achieved with ~6-9 splitting measurements (top left panel of

Figure 9a). The orientation of the starting model does affect the likelihood of uniquely identifying the anisotropy orientation. With our randomly generated starting orientations, the probability of constraining the starting orientation varies (Figure S3), but on average randomly oriented starting models do slightly worse compared to the results shown in Figure 9. For six measurements, the randomly orientated models on average find the correct orientation in 65% of all simulations, compared to Figure 9, where a non-rotated and Ppv rotated by 90° can constrain on average 75% of the simulations. As with our previous tests, it is clear that a mixture of SK(K)S and ScS shear wave splitting measurements provide the highest likelihood of constraining the starting orientation, although the optimal mix of ScS and SK(K)S depends on the starting model orientation. Our tests confirm that datasets that contain only ScS measurements (that is, SKS number of zero) cannot constrain the azimuth of the Ppv elastic tensor if its [100] axis is horizontal, due to the lack of variability in predicted fast polarization direction (Figure 2). The dependence of our results on angular dispersion of the propagation azimuths (right panels of Figure 9a) are similar to those for the case in which we attempted to retrieve the starting model; in general, a wide distribution of azimuths will increase the probability of uniquely constraining the orientation of Ppv, while datasets whose propagation azimuths are tightly clustered are less ideal. The same is generally true for the random starting models, despite some small excursions from the overall trend (Figure S3). These small excursions or “bumps” in the curves are artifacts, and are related to stochastic variations in the distribution of the predicted fast splitting directions for different models.

Next, we considered elasticity models that explicitly take into account texture development in a polycrystalline aggregate, in addition to the single-crystal elastic tensors that are the main focus of our study. While there are many uncertainties in texture models

for Ppv at lowermost mantle conditions, these models may be more representative of a realistic texture of aligned Ppv mineral grains. We only considered one case, invoking dominant slip on the (010) plane. Somewhat surprisingly, we found that for modeled Ppv LPO, there is a much lower probability of constraining the orientation of the elastic tensor than for test cases that used a single crystal elastic tensor (Figure 8a). We investigated possible reasons for this, and found that in contrast to the single-crystal models, for the textured Ppv model it is fairly common for the algorithm to identify what we term as “unstable” solutions, which are illustrated in Figure S4. In this situation, a certain orientation might fit the observations, but adjacent orientations (in which the elastic tensor is rotated by 5°) do not. This is in contrast to the behavior of single-crystal elastic models (Figure 2), in which the best-fitting orientations are adjacent to other solutions that also fit the data (in other words, the misfit values vary smoothly as a function of rotation angles of the candidate tensors). In addition, the presence of unstable solutions is highly dependent on our use of the misfit criterion of 20° . Figure S4 shows results for a range of misfit cutoff values, and demonstrates that these unstable solutions disappear with the application of more conservative misfit criteria.

We define a “stable” solution as one in which, if the elastic tensor is rotated slightly ($\sim 5^\circ$ in any direction), the rotated elastic tensor would still yield an acceptable fit to the synthetic data. In contrast, an “unstable” solution is one that has no adjacent orientations that yield an acceptable fit to the data. For the case of the textured Ppv model, the algorithm generally identifies many “unstable” orientations (Figure 9); again, this is in contrast to the generally “stable” orientations identified for single-crystal Ppv (Figure 7). In order to illustrate the effects of these unstable solutions, we applied a sensitivity cutoff to our textured Ppv simulations (Figure 8a, second row) to illustrate the effects of removing all

unstable solutions. If we consider only stable solutions, the probability of uniquely constraining the starting orientation increases by 20% on average (Figure 9a).

In order to identify the starting orientation of the Ppv LPO, we found that a mixture of SK(K)S and ScS shear wave splitting measurements again provide the highest likelihood of constraining the orientation (Figure 8a: bottom, middle panel). There is a clear dependence on angular dispersion (Figure 9a: bottom, right panel). Specifically, with low values of R (0-0.1) and middle values of R (0.5-0.7), there is a higher probability of constraining the orientation, while there is a decrease in probability between $R = 0.1$ and $R = 0.4$. In all other cases and starting models, we have not observed this pattern of dependence with R . While there is no explanation for this pattern, large values of R (0.8-1.0) resulting in low probabilities of finding the starting orientation is consistent with all other tests.

Returning to our consideration of single-crystal Ppv models, and as in section 3.2, we considered the effect of adding a reflection measurement to shear wave splitting observations to constrain the orientation of the single-crystal Ppv starting model (Figure 9b). For this test, we used a starting model that invokes an isotropic pvp layer over an anisotropic pvp layer with dominant $[100](010)$ slip (Model A in Figure 3). As in the previous test, we find that just adding one observation of reflection polarity measurements improves the probability of constraining the starting orientation (Figure 9b), although the improvement was somewhat less dramatic. Again as with the previous tests, the relative improvement is greatest for datasets with number of measurements N roughly between 5 and 9.

Finally, in a test analogous to the Gaussian noise test discussed in section 3.1 and illustrated in Figure 7c, we considered a single-crystal Ppv test in which we tried to retrieve

the correct starting orientation using synthetic observations that included random, Gaussian distributed errors on the fast polarization predictions (Figure 10). We found that adding Gaussian noise to the fast polarization directions, normally distributed between -20° and 20° with a mean of 0° and standard deviation of 9° , does not significantly hinder the probability of constraining the starting model's orientation (Figure 10a). However, this test allowed us to explore the distinction between *uniquely* constraining the starting model's orientation and identifying a model with a *minimum* misfit value that corresponds to the correct starting orientation. For the error-free synthetic datasets, the minimum misfit value always corresponds to the correct orientation, even for cases in which other orientations are allowed by the data. For cases in which Gaussian error is incorporated to the synthetic dataset; however, it is possible for the orientation with the minimum misfit value to be different from the correct solution. This observation led us to carry out a test (Figure 10b) in which rather than attempting to *uniquely* constrain the correct starting orientation, we tested whether the best-fitting orientation (that is, the candidate orientation with the minimum misfit value) actually corresponded to the correct starting orientation. We further tested whether the best-fitting solution in terms of misfit was oriented within 10° - 20° of the known, correct starting orientation. Encouragingly, we found that the probability that the minimum misfit solution was within 20° of the correct orientation exceeded 50% for datasets with a relatively small number of shear wave splitting measurements ($N \approx 4$).

4. Discussion

4.1 Implications for the interpretation of real-world data sets

Understanding the scope of information about lowermost mantle anisotropy contained in shear wave splitting and reflection polarity observations is crucial for our

ability to relate anisotropy observations to flow at the base of the mantle. While the mechanisms of lowermost mantle anisotropy remain imperfectly known, the results presented in this paper reveal observational strategies that can maximize the probability of constraining the mechanism and/or orientation, regardless of the actual anisotropic geometries present. This work shows that a diversity of shear wave splitting measurements and reflection polarity data is essential, and the modeling of single phases (e.g., ScS, SKS, SdS) is typically insufficient to constrain anisotropic geometry.

Specifically, this work demonstrates that because different seismic phases (ScS, SKS, SKKS, PdP, SdS) propagate through or reflect off the D" region at different angles from the horizontal, a combination of these phases is more useful for constraining anisotropy than datasets with wide azimuthal coverage. Consider, for example, a hypothetical case in which 9 unique splitting measurements for ScS phases are used to probe an anisotropic structure consisting of horizontal, single crystal post-perovskite. In this case, post-perovskite can only be distinguished from other plausible anisotropic models less than 10% of the time (Figure 8a and 9a). However, if SK(K)S phases and/or reflection polarities are incorporated into the analysis, then we can distinguish between the two possible mechanisms nearly 40% of the time (Figure 8a). In all cases of varying starting models and orientations, a combination of different types of data increases the probability of constraining the starting model by 10% to 60%. This pattern also generally holds true for finding the orientation of the Ppv elastic tensor. A diversity of data increases the likelihood of constraining the orientation of Ppv anisotropy anywhere from 10% to 50% for 6 unique measurements. Interestingly, we observed an exception to this (Figure 9a) for Ppv oriented at an azimuth of 90°, where only ScS splitting data (SKS number of 0) had the best chance to constrain the starting orientation.

Body wave datasets that probe seismic anisotropy in the lowermost mantle should combine both multiple data types and wide azimuthal coverage to maximize the probability that the anisotropic geometry can be tightly constrained. Figure 11 illustrates regions in the mantle in which all of the body wave measurement methods could potentially be applied simultaneously. This map was generated by considering the actual distribution of high-magnitude ($M > 6.5$) seismicity on Earth, in combination with a database of long-running broadband seismic stations beneath which the upper mantle anisotropy pattern has been shown to be simple enough to correct for (Lynner and Long, 2013, 2014b). While there are many regions of D'' with limited raypath coverage for the types of data considered in this study, we find that North America, the Arctic, northwestern Pacific, and Australia are regions that represent ideal targets to collect a diverse set of observations to further constrain D'' anisotropy.

Our results inform our view of why previous studies that included crossing raypaths (e.g., Ford et al., 2015; Creasy et al., 2017) were unable to uniquely constrain a model for D'' anisotropy. Our study indicates that a relatively large number of shear wave splitting measurements (approximately 9 or more for most cases in Figure 8a) are needed to have at least a 40% to 60% chance of uniquely identifying the starting model. The observational datasets of Ford et al. (2015) and Creasy et al. (2017) included approximately four to eight shear wave splitting measurements over unique azimuths in the lowermost mantle (Table 3). The synthetic models presented in this paper help to provide context for why these studies have not been able to uniquely constrain a particular mechanism or orientation for anisotropy (e.g. Ford et al., 2015, Creasy et al., 2017). For example, each of these studies (Table 3) had relatively high angular dispersion values for their range of predicted fast splitting directions (greater than 0.4 in all cases). As discussed in section 3.2, datasets with

lower angular dispersion values are generally more successful at constraining a unique elastic tensor. Therefore, even though many of the studies listed in Table 3 used diverse data types with combinations of SKS, SKKS, and ScS, they could not uniquely constrain an anisotropy mechanism or orientation when testing the elastic tensors considered in this study. The studies that used one type of observation (Nowacki et al., 2010; Thomas et al., 2011) did not consider all possible elastic tensors and orientations that we tested here, so we cannot directly compare them with the results of our synthetic tests. If the mechanisms for anisotropy and the associated elastic tensors can be reliably assumed, there is generally a higher chance of identifying the correct orientation and inferring the correct mantle flow geometry. With only 9 measurements, there is a 40% to 80% chance of uniquely constraining the orientation of post-perovskite (Figure 9a), an improvement from the chance of uniquely identifying the elastic tensor itself (a 40%-60% chance). Consideration of these results in future studies of D'' anisotropy, as well as a more detailed consideration of how errors and uncertainties propagate in forward models, should enhance our ability to characterize anisotropy at the base of the mantle. A more detailed statistical analysis may be required similar to this study here to fully explore the error and model space.

4.2 Practical considerations

Our tests that assumed Gaussian error on the predicted fast splitting directions (Figure 10b) demonstrate that it does not significantly affect the probability of constraining the model, as compared to noise-free synthetic data. When including Gaussian error, we found that as few as four shear wave splitting measurements can identify the correct orientation within 20° more than 50% of the time. Datasets of this size (roughly four unique measurements in the same region of D'') can likely be reasonably achieved in many regions

of the lowermost mantle, based on the distribution of available raypaths (Figure 11). This finding may help with the interpretation of modeling results for real splitting datasets, such as those considered by Ford et al. (2015) and Creasy et al. (2017), for which multiple possible anisotropic orientations were identified, but particular orientations had significantly lower misfit values than others.

Our synthetic modeling results also shed light on potential complications in interpretation caused by the different symmetry classes of some of the candidate elasticity scenarios that have been proposed to explain lowermost mantle anisotropy. To effectively differentiate these scenarios using shear wave splitting data alone, it is crucial for splitting datasets to probe the symmetry of the mineral such that no other elastic tensor simulates that pattern for a similar range of propagation directions. Of the candidate scenarios we tested in this study, Fp has the highest (cubic) symmetry with only 3 unique constants in the elastic tensor. SPO models have the next highest symmetry, since tubule and oblate SPO models are hexagonal (transversely isotropic) with 5 unique elastic constants. Ppv and Br are both orthorhombic, with the same order of symmetry and only 9 unique elastic constants. In more complicated models, like LPO calculations of single crystals, the symmetry is much lower than its single crystal counterpart with 21 unique elastic constants.

4.3 Limitations of our modeling approach

We caution that our synthetic tests must be interpreted in light of the still-considerable limitations in our understanding of the elasticity of anisotropic materials at lowermost mantle conditions. We have focused mainly on single-crystal elastic tensors, derived mainly from ab initio simulations, as a reasonable starting point in this study; however, predictions of single-crystal elasticity are likely imperfect and do not take into

account effects such as variation in composition. Furthermore, single-crystal elasticity is an imperfect proxy for the likely anisotropic geometry of polycrystalline aggregates, particularly for minerals with high symmetry such as Fp (e.g., Yamazaki and Karato, 2002). The further consideration of elasticity models that explicitly take into account texture development will be an important step, although texture models include a number of poorly known parameters (such as activation energies for different slip systems) and consensus on the dominant slip systems in different lowermost mantle minerals remains elusive (e.g., Nowacki et al., 2011).

Another limitation of the work proposed here is that it is carried out in the context of ray theoretical predictions, assuming infinite frequency, rather than considering the full characteristics of the waveform at finite frequencies. With improvements on both observational and modeling techniques that model the full waveform (e.g., Kawai and Geller, 2010, Nowacki and Wookey, 2016, Parisi et al., 2018), the interpretation of seismic anisotropy observations can very likely be improved. In particular, future work must investigate how the measurement techniques used influence the interpretation of finite frequency waveform effects and to what extent ray theoretical predictions are a useful approximation. Despite these limitations, we expect that future work that predicts body wave observations in the presence of lowermost mantle anisotropy in a finite-frequency framework will likely find similar results: a diversity of seismic phases and measurement yields the best probability of capturing the symmetry, orientation, and properties of an elastic tensor. While this study is limited to a specific set of currently-available elastic tensors from the mineral physics literature, our overall findings should be generally applicable and adaptable to future improvements of our knowledge of lowermost mantle elasticity.

5. Summary

To summarize, the complete characterization and interpretation of seismic anisotropy at the base of the mantle would have profound effects on our understanding of lower mantle dynamics, potentially yielding insights into the pattern of mantle flow. Many recent studies have pointed to the difficulty of distinguishing different models of lowermost mantle anisotropy with body wave observations, given challenges with data coverage and uncertainties in the mechanism for anisotropy and the relationships between deformation and the resulting anisotropy at lower mantle conditions. In this study, we conducted a series of Monte Carlo simulations to determine what combination of body wave datasets (shear wave splitting and reflection polarities) are required to constrain D'' anisotropy. We tested various starting models, orientations, and methods for the detection and identification of D'' anisotropy. The modeling approach in this study is applicable to a wide range of elasticity models, and can be extended as our knowledge of the physical properties of the lowermost mantle increases. This approach can be used in future work on D'' anisotropy to further explore how well a dataset can discriminate among possible elastic tensors.

Our results show that a diversity of observational techniques, including different types of seismic phases propagating over a range of raypath directions, are necessary in order to maximize the chances of constraining anisotropy at the base of the mantle. A combination of shear wave splitting measurements and observations of PdP and SdS reflection polarities in the same regions may be particularly powerful. We have further shown that if the mineralogy and/or mechanism for anisotropy can be constrained from independent data, then the orientation of the elastic tensor (and thus information about

766 patterns of mantle flow) can likely be retrieved from observational datasets that include a
767 relatively modest number of measurements.

Tables

Table 1

Summary of all elastic tensors used in the forward modeling. Columns show the type of tensor (single-crystal, LPO based on experimental data, SPO based on effective medium averaging, or LPO based on global flow and texture models), the phases and/or constituents, and the reference. For the single-crystal tensors, the pressure and temperature conditions used in the modeling are also indicated. ¹Elastic tensors used for tests to uniquely constrain the starting model. ²Elastic tensors used for tests to uniquely constrain the orientation.

Single Crystal Tensors				
Geometry	Phase	Pressure (GPa)	Temperature (K)	References
Single Crystal	Br ¹	125	2500	<i>Wentzcovitch et al.</i> [2006], <i>Wookey et al.</i> [2005a, 2005b]
		126	2800	
		136	4000	
	Ppv ^{1,2}	135	4000	<i>Stackhouse et al.</i> [2005]
	MgO ¹	135	3000	<i>Karki et al.</i> [1999]
Other Tensors				
Geometry	Phase	Notes		References
Experimental LPO	MgO ¹	P = 0.3 GPa; T = 1473K		<i>Long et al.</i> [2006]
SPO ¹	0.003 vol. fraction melt	Oblate shape		<i>Walker and Wookey</i> [2012]
	0.003 vol. fraction melt	Tubule shape		<i>Walker and Wookey</i> [2012]
Calculated LPO ²	Ppv	TX2008-V1 model; dominant slip plane: (010), P = 125-136; T = 3000-4000 K		<i>Walker et al.</i> [2011]; Tensors based on <i>Stackhouse et al.</i> , [2005] and <i>Stackhouse and Brodholt</i> [2007]

Table 2

Models for the top (isotropic) and bottom (anisotropic) layers of each model described in Figure 3 for reflection polarity models. The dominant slip system assumed in each bottom layer is listed.

Model	Top Layer (isotropic)	Bottom Layer (anisotropic)	Slip System	References
A	Ppv	Ppv	[100](010)	<i>Walte et al. [2009]</i> <i>Wentzcovitch et al. [2006]</i>
B	Br	Ppv	[100](010)	<i>Walte et al. [2009]</i> <i>Wentzcovitch et al. [2006]</i>
C	Br	Br	[010](100)	<i>Stackhouse et al. [2005]</i> <i>Mainprice et al. [2008]</i>
D	Fp	Fp	[100](001)	<i>Karki et al. [1999]</i>

Table 3

Summary of previous studies that have used crossing raypaths to study D'' anisotropy, as identified in Figure 1. The number of unique azimuths is given; each azimuth typically contains multiple observations (in practice, these observations are typically averaged for each set of raypaths). SKS number is calculated as defined in the text; for example, Nowacki et al. (2010) used only ScS phases, therefore the SKS number is 0. Angular dispersion (R) of the raypath azimuths is also calculated as described in the text.

References	Region	Number of Unique Azimuths	SKS Number	R
Creasy et al., 2017	New Zealand	8	0.75	0.7866
Creasy et al., 2017	SW Australia	4	0.5	0.4297
Ford et al., 2015	Afar Peninsula	5	0.6	0.8305
Thomas et al., 2011	Siberia + Caribbean	4	reflection polarities	0.5801
Nowacki et al., 2010	Caribbean	6	0	0.5734

Figure Captions

Figure 1. Summary map of previously published studies (which include shear wave splitting measurements and reflection polarity observations) to constrain D" anisotropy, updated and adapted from Nowacki et al. (2011). Highlighted areas (pink/gray) indicate regions that have been probed for D" anisotropy with these methods. Regions in pink indicate studies that used multiple techniques and/or intersecting ray paths, for which at least two observations intersect in the same region with different propagation azimuths. Two such studies are highlighted on the right. Panel (a) shows the raypaths (black lines) beneath Siberia studied in the reflection polarity study of Thomas et al. (2011). CMB bounce points are indicated with diamonds and circles, and the dotted arrow indicates paleo subduction direction 100 Ma ago of the Kula plate. Background colors indicate P wave velocity deviations at the base of the mantle from the model of Kárason and Hilst (2001). Panel (b) shows a schematic diagram of shear wave splitting measurements of SKS (green), SKKS (red), and ScS (blue) phases beneath the Afar region of Africa (Ford et al., 2015). Background colors show S wave velocity deviations at a depth of 250 km above core mantle boundary from the GyPSuM tomography model (Simmons et al., 2010).

Figure 2. Elastic properties of models from Table 1 for D" anisotropy tested in this study, as expressed in the predicted shear wave splitting behavior. Predicted shear wave splitting behavior is shown as a 3D spherical representation relative to geographic space, with the [100], [010], and [001] axes indicated in order to view the variation of splitting of SKS, SKKS, and ScS with azimuth. The anisotropy 3-D spheres show the directional dependence of seismic anisotropy (strength [gray color bar] and fast-axis directions [black bars]). For each model, the [100] and [010] axes are parallel to the CMB and oriented north

and west, respectively. Black bars show predicted splitting over a range inclinations and azimuths, as computed using the MSAT toolkit (Walker and Wookey, 2012). Magenta bars illustrate the predicted fast polarization directions for the given starting models for a particular set of SKS, SKKS, and ScS raypaths every 20° (we actually use steps of 5° in the synthetic modeling, but the plotting is too dense to show) that are evenly distributed. Inclination angles used in the modeling are based on the average inclination angles for each phase through the D" layer; we assume that ScS propagates nearly horizontally through the lowermost mantle, as described in the text. From left to right, we show elastic tensor models for single-crystal Ppv (Stackhouse et al., 2005), single-crystal Br (Wentzcovitch et al., 2006), single-crystal Fp (Karki et al., 1999: Labeled as "Fp (Karki)"), experimentally-derived LPO of Fp (Long et al., 2006: Labeled as "Fp (Long)"), Oblate SPO (Walker and Wookey, 2012), Tubule SPO (Walker and Wookey, 2012), and the averaged, textured Ppv (Walker et al., 2011). Background colors are %S-wave anisotropy.

Figure 3. Predictions of reflection polarities for PdP and SdS waves for different D" anisotropy models shown as an upper hemispherical projection since polarities depend on azimuth, not inclination as in Figure 2. Predictions are made as a function of azimuth and epicentral distance (from 60° to 80°). Azimuth is relative to the slip direction (indicated by the black arrow), which also corresponds to direction of lowermost mantle flow for a simple horizontal shear geometry. The first two columns show the reflection coefficients of P-P and SH-SH upon reflection off the D" discontinuity, located 300 km above the core mantle boundary in the model. Blue and red regions indicate positive and negative polarities, respectively. Models A, C, and D illustrate situations where there is an onset of anisotropy at the D" discontinuity while Model B invokes both a phase change (from Br to

Ppv) and the onset of anisotropy. The last column illustrates the predicted S wave anisotropy (color bar) and predicted shear wave splitting fast directions (black bars) for the same models, plotted as a function of azimuth and inclination from the horizontal. Elastic tensors corresponding to these models are shown in Table 2.

Figure 4. Flow chart of steps in our modeling framework. The first step is to identify the starting model and its orientation from Tables 1 or 2. Secondly, randomly choose an azimuthal distribution of raypaths through the starting model and fix the SKS number. Thirdly, use the raypaths from step 2 and calculate the fast polarization directions and/or reflection polarities (splitting parameters) based on the identified starting model and SKS number. Fourth, use this synthetic dataset to use the forward modeling approach to identify which models and orientations fit the synthetic dataset. We apply the misfit cutoff as described in Methods to eliminate certain models and orientations in order to see if the synthetic dataset can uniquely constrain the starting model. Lastly, in step 5, we repeat this same process M times (number of iterations), identifying a new random distribution of raypaths each time.

Figure 5. An illustrative example of how shear wave splitting predictions for an individual iteration in our stochastic modeling scheme are calculated. (a) Plane view (looking down from above on CMB) of starting model for Ppv (Stackhouse et al., 2005) showing S wave % anisotropy (colors), with fast polarization directions plotted as black bars. (b) Raypath distribution for this example for SKS (red), SKKS (orange), and ScS (blue), plotted as azimuth from north. (c) The predicted fast polarization directions based on the starting model in (a) and the raypath distribution in (b). Colors indicate phase type.

866

867 Figure 6. Results of a test of how many iterations are needed for the model results
868 to converge. The x-axis defines the number of iterations (M) (that is, number of unique
869 raypath configurations with similar characteristics) that were successively carried out. The
870 y-axis indicates what percentage of the iterations run could be uniquely constrained. This
871 particular test used 9 shear wave splitting measurements and a starting model of horizontal
872 Ppv, and we found that after a large number of iterations, the starting model could be
873 constrained for 41% of all iterations carried out. In contrast, for the other 59%, a unique
874 solution of Ppv could not be constrained for that particular synthetic dataset. Based on the
875 results of this test, at least 5,000 iterations were carried out for each test described in this
876 study.

877

878 Figure 7. An example of how the forward modeling method identifies all possible
879 orientations of the Ppv single crystal elastic tensor that fit a particular synthetic dataset. We
880 show two synthetic datasets of 8 (a) and 4 (b) unique synthetic measurements with 3 SKS,
881 3 SKKS, 2 ScS measurements and 1 SKS, 2 SKKS, and 1 ScS measurements, respectively.
882 The last case (c) shows a test with the same 4 synthetic measurements as in (b) but with
883 Gaussian distributed random error to the predicted fast directions. These projections show
884 all possible permissible orientations (colored dots) of the Ppv tensor for the given synthetic
885 dataset plotted as an upper hemispherical projection of the [100], [010], and [001] axes.
886 The white dots mark local minima, where the magenta dots represent the global minimum.
887 The magenta dots indicate the global minimum misfit, which should be equal to a non-
888 rotated Ppv (that is, horizontal [100] and [010] axes and vertical [001] axis).

889

Figure 8: Results of synthetic tests that aim to uniquely constrain the starting model/mechanism, as discussed in section 3.2. Three different sets of tensors were tested, while three different aspects of the raypath configuration were varied. In (a), each row shows plots of the probability of uniquely identifying the given starting model (Ppv, Br, and MgO). Each column represents the variable describing raypath configuration that was allowed to vary, while the other two were fixed. In the first column, we varied the number of measurements N , but fixed the SKS ratio (0.67) and tested the full range of possible R values. In the second column, we varied SKS number but fixed the number of measurements ($N = 9$) and tested the full range of possible R values. In the third column, we varied the angular dispersion R , but fixed the number of measurements and SKS number ($N = 9$ and $SKS = 0.6$). We further tested a range of starting orientations for each starting model (three for Ppv and Br, two for Fp); the labels (0, 45, 90) refer to the rotation angle (in degrees) about the [100] axis from the horizontal. In (b), we chose Model A in Figure 3 as the starting model and tested whether we could uniquely constrain this starting model using a combination of shear wave splitting and reflection measurements. For this test, the SKS number was fixed (0.67) and we tested the full range of possible angular dispersion values. The test shown in (b: left image) compares synthetic datasets with only shear wave splitting measurements (black line, SS) to those that include splitting plus one additional reflection measurement for a P and S reflected phase off the D'' over a randomly defined azimuth (gray line, SS+R). The difference in probability between these two raypath configuration scenarios is shown in right image.

Figure 9. Results of synthetic tests that aim to uniquely constrain the orientation of a Ppv starting model, as discussed in section 3.3. In (a), each row shows plots of the

probability of uniquely identifying the given starting model's orientation using the synthetic data, for three different orientations about the [100] axis in the starting model, as shown in the legend (with the labels 0 and 90, referring to the angle about the [100] axis) and described in the text. As in Figure 7, each column represents the variable that was allowed to vary, while the other two were fixed. The second row illustrates the results of tests that aimed to uniquely constraining the starting model orientation for textured Ppv models invoking slip on the (010) plane (Walker et al., 2011). For these tests, we distinguish between scenarios in which we increased the sensitivity (that is, discarded "unstable" solutions, as described in the text). Tests in which unstable solutions were discarded (gray line) increased the probability of identifying the orientation of anisotropy in comparison to retaining unstable solutions (black line). In (b), we show results of tests of the effect of adding one additional reflection measurement to the shear wave splitting measurements, using Model A in Figure 3 as the starting model. For these tests, the SKS number was fixed (0.67) and we tested the full range of possible angular dispersion values. The test shown in (b: left image) compares synthetic datasets with only shear wave splitting measurements (black line, SS) to those that include splitting plus one additional reflection measurement for a P and S reflected phase off the D" over a randomly defined azimuth (gray line, SS+R). The difference in probability between these two raypath configuration scenarios is shown at right.

Figure 10: Results of tests that aimed to uniquely identify the orientation of a single-crystal Ppv starting model, with Gaussian distributed random errors (standard deviation = 9°) incorporated into the synthetic shear wave splitting dataset. In (a), we varied the number of shear wave splitting measurements and calculated the probabilities of correctly

retrieving the starting model orientation. In (b), we plot the probability of correctly identifying the starting orientation for a synthetic dataset with Gaussian error applied based on an identification of the minimum misfit (as opposed to searching for a unique solution). In (b), the black line (unique solution, same as in (a)) shows the probability of uniquely constraining the orientation of the starting model. The other two lines show the probability of identifying the correct solution within 10° or 20° by using the minimum misfit.

Figure 11. Map of regions of the lowermost mantle in which the various measurement methods (SKS [distance range: $108^\circ - 122^\circ$], SKKS [$108^\circ - 122^\circ$], and ScS [$60^\circ - 80^\circ$] shear wave splitting and reflection polarities) used in this study could potentially be applied. We parameterize the D'' layer into a 5° by 5° grid. We calculated raypaths for different seismic phases using TauP (Crotwell et al., 1999) assuming a 250km thick D'' layer. We used a set of seismic stations with simple upper mantle anisotropy (Lynner and Long, 2013, 2014b) for all events greater than Mw6.5 that occurred in the time span of deployment for each seismic station for SKS, SKKS, and ScS. For reflection polarities, we considered only dense arrays openly available: TAMNNET, POLENET, GAMSEIS, Yellowknife Array, KNET, Southern California Network, GRSN Array, F-Net, USArray (using stations in Alaska), USArray (using stations in Texas), USArray (using stations in Minnesota), USArray (using stations in New York), USArray (using stations in South Carolina), and the Pacific Northwest Seismic Network.

Acknowledgements

This work was supported by a National Science Foundation (NSF) Graduate Research Fellowship grant DGE-1122492 to N.C. and by NSF grant EAR-1547499 to M.D.L. Some

962 figures were prepared using the Generic Mapping Tools (Wessel and Smith, 1991). We
963 thank the Yale Center for Research Computing for guidance and use of the research
964 computing infrastructure, specifically Kaylea Nelson. AP received funding from the
965 European Union's Horizon 2020 research and innovation program under the Marie
966 Sklodowska-Curie grant agreement No 642029 - ITN CREEP. We are grateful to Sanne
967 Cottaar, Jeroen Ritsema, and editor Ana Ferreira for thoughtful and constructive comments
968 that helped us to improve the paper.

References

- Bendat, J.S., Piersol, A.G., 2011. Random Data: Analysis and Measurement Procedures. John Wiley & Sons.
- Cottaar, S., Romanowicz, B., 2013. Observations of changing anisotropy across the southern margin of the African LLSVP. *Geophys. J. Int.* ggt285. <https://doi.org/10.1093/gji/ggt285>
- Creasy, N., Long, M.D., Ford, H.A., 2017. Deformation in the lowermost mantle beneath Australia from observations and models of seismic anisotropy. *J. Geophys. Res. Solid Earth* 122, 2016JB013901. <https://doi.org/10.1002/2016JB013901>
- Crotwell, H.P., Owens, T.J., Ritsema, J., 1999. The TauP Toolkit: Flexible Seismic Travel-time and Ray-path Utilities. *Seismol. Res. Lett.* 70, 154–160. <https://doi.org/10.1785/gssrl.70.2.154>
- Deng, J., Long, M.D., Creasy, N., Wagner, L., Beck, S., Zandt, G., Tavera, H., Minaya, E., 2017. Lowermost mantle anisotropy near the eastern edge of the Pacific LLSVP: constraints from SKS–SKKS splitting intensity measurements. *Geophys. J. Int.* 210, 774–786. <https://doi.org/10.1093/gji/ggx190>
- Ford, H.A., Long, M.D., 2015. A regional test of global models for flow, rheology, and seismic anisotropy at the base of the mantle. *Phys. Earth Planet. Inter.* 245, 71–75. <https://doi.org/10.1016/j.pepi.2015.05.004>
- Ford, H.A., Long, M.D., He, X., Lynner, C., 2015. Lowermost mantle flow at the eastern edge of the African Large Low Shear Velocity Province. *Earth Planet. Sci. Lett.* 420, 12–22. <https://doi.org/10.1016/j.epsl.2015.03.029>
- Ford R., Garnero Edward J., McNamara Allen K., 2006. A strong lateral shear velocity gradient and anisotropy heterogeneity in the lowermost mantle beneath the southern Pacific. *J. Geophys. Res. Solid Earth* 111. <https://doi.org/10.1029/2004JB003574>
- Garnero, E.J., McNamara, A.K., Shim, S.-H., 2016. Continent-sized anomalous zones with low seismic velocity at the base of Earth’s mantle. *Nat. Geosci.* 9, 481–489. <https://doi.org/10.1038/ngeo2733>
- Goryaeva, A.M., Carrez, P., Cordier, P., 2017. Modeling defects and plasticity in MgSiO₃ post-perovskite: Part 3—Screw and edge [001] dislocations. *Phys. Chem. Miner.* 44, 521–533. <https://doi.org/10.1007/s00269-017-0879-0>
- Groos, J.C., Ritter, J.R.R., 2009. Time domain classification and quantification of seismic noise in an urban environment. *Geophys. J. Int.* 179, 1213–1231. <https://doi.org/10.1111/j.1365-246X.2009.04343.x>
- Guest, W.S., Kendall, J.M., 1993. Modeling seismic waveforms in anisotropic media using maslov asymptotic theory. *J. Explor. Geophys.* 29, 78–92.
- Kárason, H., Hilst, R.D. van der, 2001. Tomographic imaging of the lowermost mantle with differential times of refracted and diffracted core phases (PKP, Pdiff). *J. Geophys. Res. Solid Earth* 106, 6569–6587. <https://doi.org/10.1029/2000JB900380>
- Karki, B.B., Wentzcovitch, R.M., Gironcoli, S. de, Baroni, S., 1999. First-Principles Determination of Elastic Anisotropy and Wave Velocities of MgO at Lower

1016 Mantle Conditions. *Science* 286, 1705–1707.
1017 <https://doi.org/10.1126/science.286.5445.1705>
1018 Kawai, K., Geller, R.J., 2010. The vertical flow in the lowermost mantle beneath the
1019 Pacific from inversion of seismic waveforms for anisotropic structure. *Earth*
1020 *Planet. Sci. Lett.* 297, 190–198. <https://doi.org/10.1016/j.epsl.2010.05.037>
1021 Kendall, J.-M., Silver, P.G., 1998. Investigating Causes of D'' Anisotropy, in: *The Core-*
1022 *Mantle Boundary Region*. American Geophysical Union, Washington D.C., pp.
1023 409–412.
1024 Lay T., Helmberger D.V., 1983. The shear-wave velocity gradient at the base of the
1025 mantle. *J. Geophys. Res. Solid Earth* 88, 8160–8170.
1026 <https://doi.org/10.1029/JB088iB10p08160>
1027 Lee, K.K.M., O'Neill, B., Panero, W.R., Shim, S.-H., Benedetti, L.R., Jeanloz, R., 2004.
1028 Equations of state of the high-pressure phases of a natural peridotite and
1029 implications for the Earth's lower mantle. *Earth Planet. Sci. Lett.* 223, 381–393.
1030 <https://doi.org/10.1016/j.epsl.2004.04.033>
1031 Long Maureen D., Lynner Colton, 2015. Seismic anisotropy in the lowermost mantle
1032 near the Perm Anomaly. *Geophys. Res. Lett.* 42, 7073–7080.
1033 <https://doi.org/10.1002/2015GL065506>
1034 Long, M.D., 2009. Complex anisotropy in D'' beneath the eastern Pacific from SKS–
1035 SKKS splitting discrepancies. *Earth Planet. Sci. Lett.* 283, 181–189.
1036 <https://doi.org/10.1016/j.epsl.2009.04.019>
1037 Long, M.D., Xiao, X., Jiang, Z., Evans, B., Karato, S., 2006. Lattice preferred orientation
1038 in deformed polycrystalline (Mg,Fe)O and implications for seismic anisotropy in
1039 D'' . *Phys. Earth Planet. Inter.* 156, 75–88.
1040 <https://doi.org/10.1016/j.pepi.2006.02.006>
1041 Lynner, C., Long, M.D., 2014a. Lowermost mantle anisotropy and deformation along the
1042 boundary of the African LLSVP. *Geophys. Res. Lett.* 41, 2014GL059875.
1043 <https://doi.org/10.1002/2014GL059875>
1044 Lynner, C., Long, M.D., 2014b. Sub-slab anisotropy beneath the Sumatra and circum-
1045 Pacific subduction zones from source-side shear wave splitting observations.
1046 *Geochem. Geophys. Geosystems* 15, 2262–2281.
1047 <https://doi.org/10.1002/2014GC005239>
1048 Lynner, C., Long, M.D., 2013. Sub-slab seismic anisotropy and mantle flow beneath the
1049 Caribbean and Scotia subduction zones: Effects of slab morphology and
1050 kinematics. *Earth Planet. Sci. Lett.* 361, 367–378.
1051 <https://doi.org/10.1016/j.epsl.2012.11.007>
1052 Mardia, K.V., Jupp, P.E., 2000. *Directional statistics*. Wiley.
1053 McNamara, A.K., Karato, S.-I., van Keken, P.E., 2001. Localization of dislocation creep
1054 in the lower mantle: implications for the origin of seismic anisotropy. *Earth*
1055 *Planet. Sci. Lett.* 191, 85–99. [https://doi.org/10.1016/S0012-821X\(01\)00405-8](https://doi.org/10.1016/S0012-821X(01)00405-8)
1056 Meade, C., Silver, P.G., Kaneshima, S., 1995. Laboratory and seismological observations
1057 of lower mantle isotropy. *Geophys. Res. Lett.* 22, 1293–1296.
1058 <https://doi.org/10.1029/95GL01091>
1059 Mitrovica, J.X., Forte, A.M., 2004. A new inference of mantle viscosity based upon joint
1060 inversion of convection and glacial isostatic adjustment data. *Earth Planet. Sci.*
1061 *Lett.* 225, 177–189. <https://doi.org/10.1016/j.epsl.2004.06.005>

1062 Murakami, M., Hirose, K., Kawamura, K., Sata, N., Ohishi, Y., 2004. Post-Perovskite
 1063 Phase Transition in MgSiO₃. *Science* 304, 855–858.
 1064 <https://doi.org/10.1126/science.1095932>
 1065 Nowacki, A., Wookey, J., 2016. The limits of ray theory when measuring shear wave
 1066 splitting in the lowermost mantle with ScS waves. *Geophys. J. Int.* 207, 1573–
 1067 1583. <https://doi.org/10.1093/gji/ggw358>
 1068 Nowacki, A., Wookey, J., Kendall, J.-M., 2011. New advances in using seismic
 1069 anisotropy, mineral physics and geodynamics to understand deformation in the
 1070 lowermost mantle. *J. Geodyn.* 52, 205–228.
 1071 <https://doi.org/10.1016/j.jog.2011.04.003>
 1072 Nowacki, A., Wookey, J., Kendall, J.-M., 2010. Deformation of the lowermost mantle
 1073 from seismic anisotropy. *Nature* 467, 1091–1094.
 1074 <https://doi.org/10.1038/nature09507>
 1075 Parisi, L., Ferreira, A.M.G., Ritsema, J., 2018. Apparent Splitting of S Waves
 1076 Propagating Through an Isotropic Lowermost Mantle. *J. Geophys. Res. Solid*
 1077 *Earth* 123. <https://doi.org/10.1002/2017JB014394>
 1078 Simmons, N.A., Forte, A.M., Boschi, L., Grand, S.P., 2010. GyPSuM: A joint
 1079 tomographic model of mantle density and seismic wave speeds. *J. Geophys. Res.*
 1080 *Solid Earth* 115, B12310. <https://doi.org/10.1029/2010JB007631>
 1081 Simmons, N.A., Forte, A.M., Grand, S.P., 2009. Joint seismic, geodynamic and mineral
 1082 physical constraints on three-dimensional mantle heterogeneity: Implications for
 1083 the relative importance of thermal versus compositional heterogeneity. *Geophys.*
 1084 *J. Int.* 177, 1284–1304. <https://doi.org/10.1111/j.1365-246X.2009.04133.x>
 1085 Simmons, N.A., Myers, S.C., Johannesson, G., Matzel, E., Grand, S.P., 2015. Evidence
 1086 for long-lived subduction of an ancient tectonic plate beneath the southern Indian
 1087 Ocean. *Geophys. Res. Lett.* 42, 2015GL066237.
 1088 <https://doi.org/10.1002/2015GL066237>
 1089 Stackhouse, S., Brodholt, J.P., Wookey, J., Kendall, J.-M., Price, G.D., 2005. The effect
 1090 of temperature on the seismic anisotropy of the perovskite and post-perovskite
 1091 polymorphs of MgSiO₃. *Earth Planet. Sci. Lett.* 230, 1–10.
 1092 <https://doi.org/10.1016/j.epsl.2004.11.021>
 1093 Thomas, C., Wookey, J., Brodholt, J., Fieseler, T., 2011a. Anisotropy as cause for
 1094 polarity reversals of D'' reflections. *Earth Planet. Sci. Lett.* 307, 369–376.
 1095 <https://doi.org/10.1016/j.epsl.2011.05.011>
 1096 Thomas, C., Wookey, J., Simpson M., 2007. D'' anisotropy beneath Southeast Asia.
 1097 *Geophys. Res. Lett.* 34. <https://doi.org/10.1029/2006GL028965>
 1098 Walker, A.M., Forte, A.M., Wookey, J., Nowacki, A., Kendall, J.-M., 2011. Elastic
 1099 anisotropy of D'' predicted from global models of mantle flow. *Geochem.*
 1100 *Geophys. Geosystems* 12, Q10006. <https://doi.org/10.1029/2011GC003732>
 1101 Walker, A.M., Wookey, J., 2012. MSAT—A new toolkit for the analysis of elastic and
 1102 seismic anisotropy. *Comput. Geosci.* 49, 81–90.
 1103 <https://doi.org/10.1016/j.cageo.2012.05.031>
 1104 Walte, N.P., Heidelbach, F., Miyajima, N., Frost, D.J., Rubie, D.C., Dobson, D.P., 2009.
 1105 Transformation textures in post-perovskite: Understanding mantle flow in the D
 1106 '' layer of the Earth. *Geophys. Res. Lett.* 36, L04302.
 1107 <https://doi.org/10.1029/2008GL036840>

1108 Wang, Y., Wen, L., 2007. Geometry and P and S velocity structure of the “African
1109 Anomaly.” *J. Geophys. Res. Solid Earth* 112, B05313.
1110 <https://doi.org/10.1029/2006JB004483>

1111 Wentzcovitch, R.M., Tsuchiya, T., Tsuchiya, J., 2006. MgSiO₃ postperovskite at D’’
1112 conditions. *Proc. Natl. Acad. Sci. U. S. A.* 103, 543–546.
1113 <https://doi.org/10.1073/pnas.0506879103>

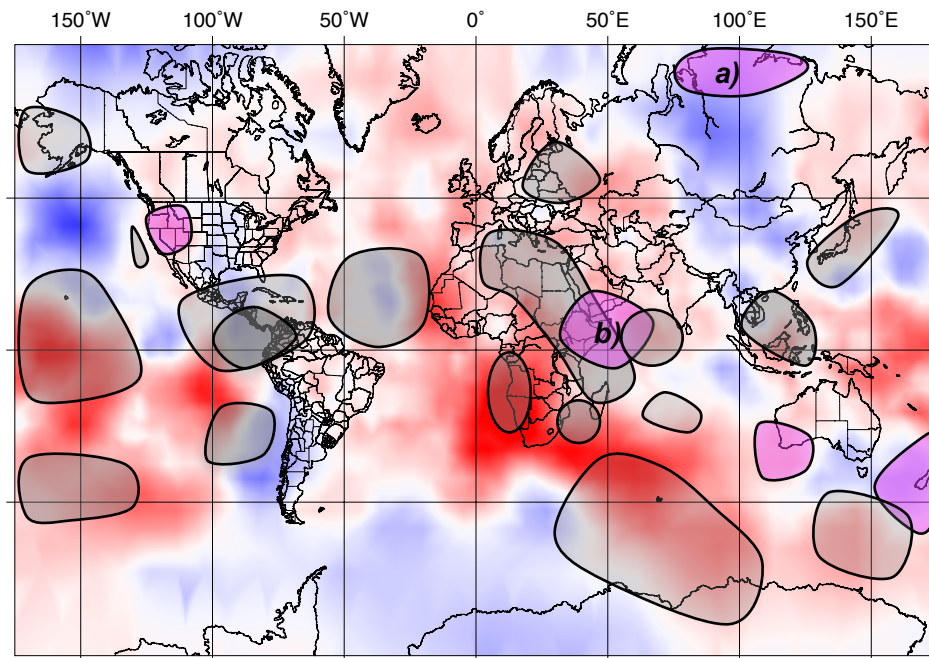
1114 Wookey, J., Kendall, J.-M., 2008. Constraints on lowermost mantle mineralogy and
1115 fabric beneath Siberia from seismic anisotropy. *Earth Planet. Sci. Lett.* 275, 32–
1116 42. <https://doi.org/10.1016/j.epsl.2008.07.049>

1117 Wookey, J., Kendall, J.-M., Rumpker, G., 2005a. Lowermost mantle anisotropy beneath
1118 the north Pacific from differential S—ScS splitting. *Geophys. J. Int.* 161, 829–
1119 838. <https://doi.org/10.1111/j.1365-246X.2005.02623.x>

1120 Wookey, J., Stackhouse, S., Kendall, J.-M., Brodholt, J., Price, G.D., 2005b. Efficacy of
1121 the post-perovskite phase as an explanation for lowermost-mantle seismic
1122 properties. *Nature* 438, 1004–1007. <https://doi.org/10.1038/nature04345>

1123 Yamazaki, D., Yoshino, T., Ohfuji, H., Ando, J., Yoneda, A., 2006. Origin of seismic
1124 anisotropy in the D’’ layer inferred from shear deformation experiments on post-
1125 perovskite phase. *Earth Planet. Sci. Lett.* 252, 372–378.
1126 <https://doi.org/10.1016/j.epsl.2006.10.004>

1127



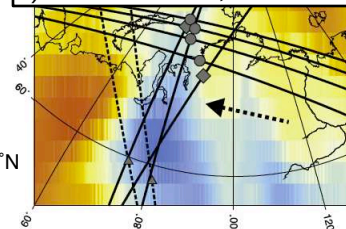
Max = 2.5



Other D'' anisotropy studies

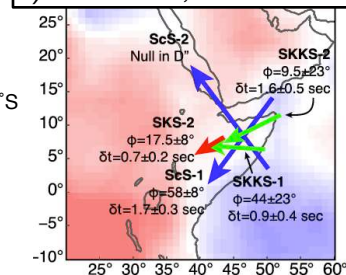
Intersecting paths

a) Thomas et al., 2011

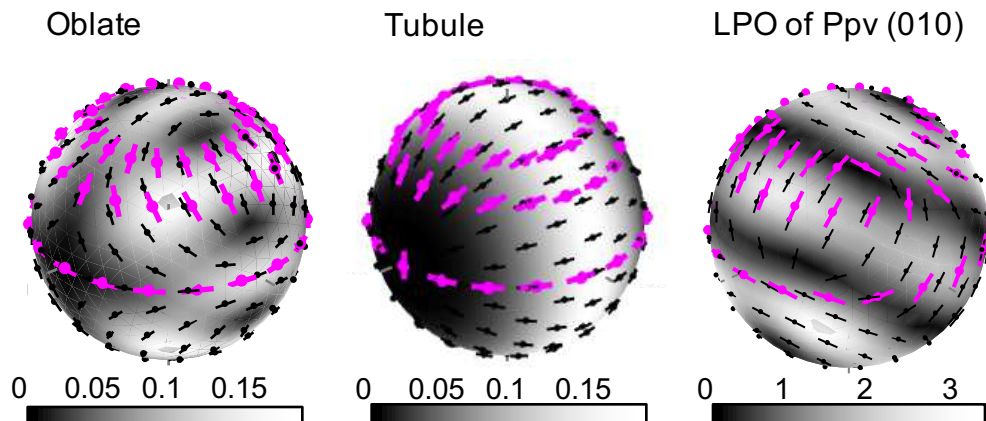
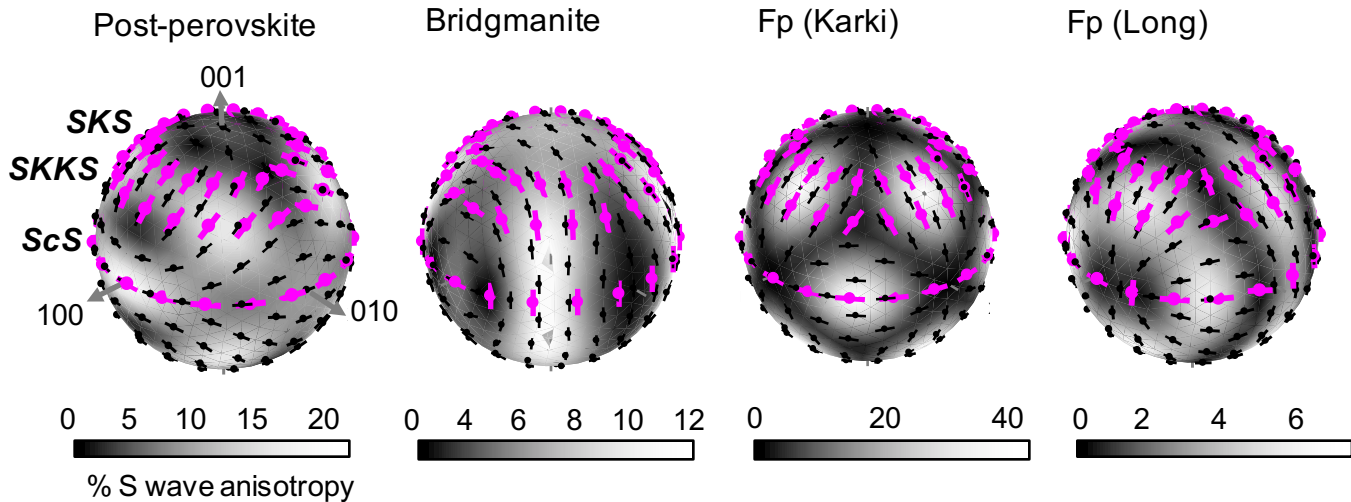


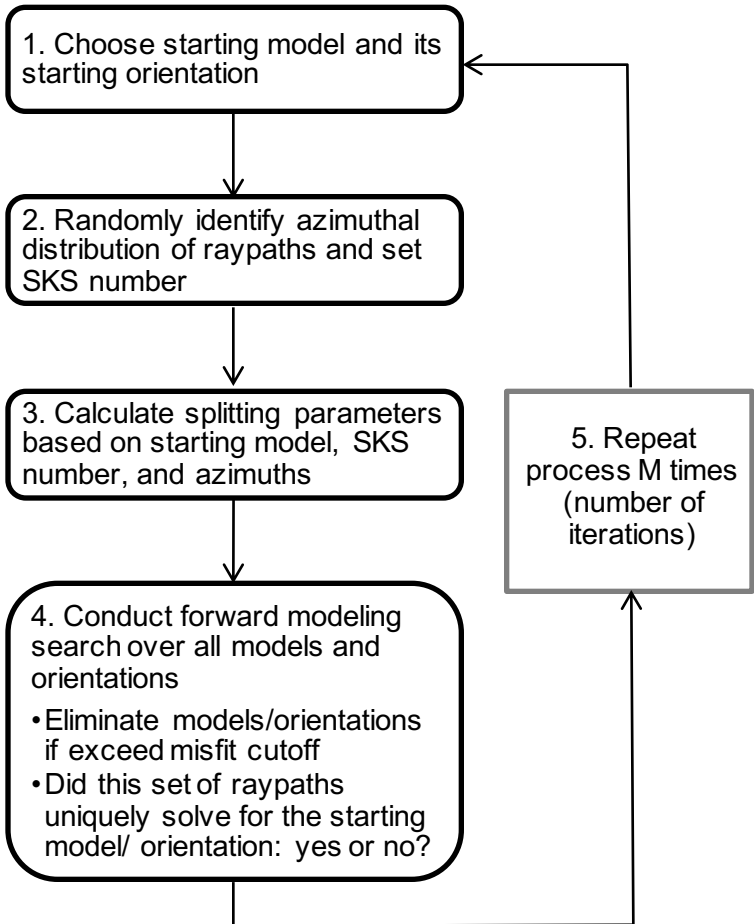
Max = 2.0

b) Ford et al., 2015

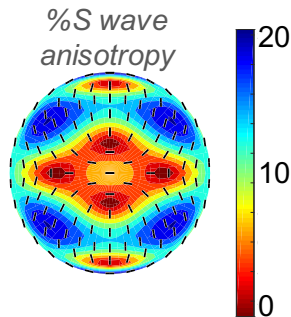


Max = 1.5

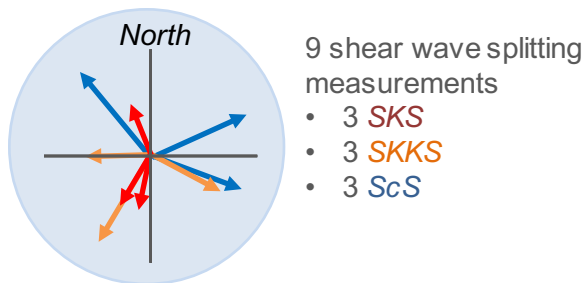




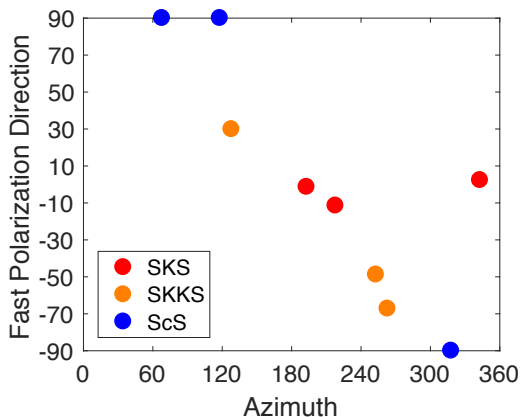
a) Starting Model

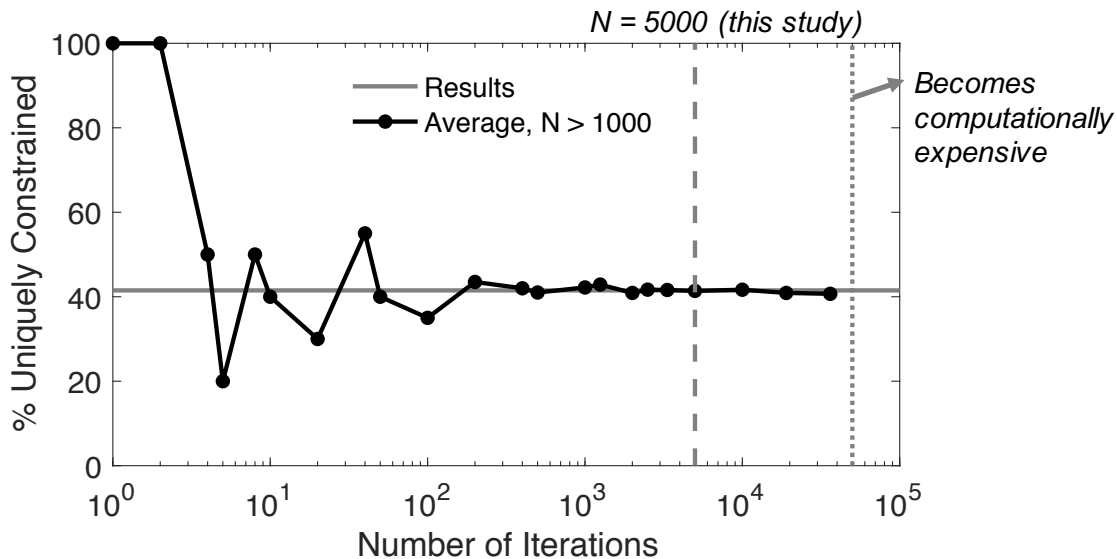


b) Select Number of Observations and their Azimuths

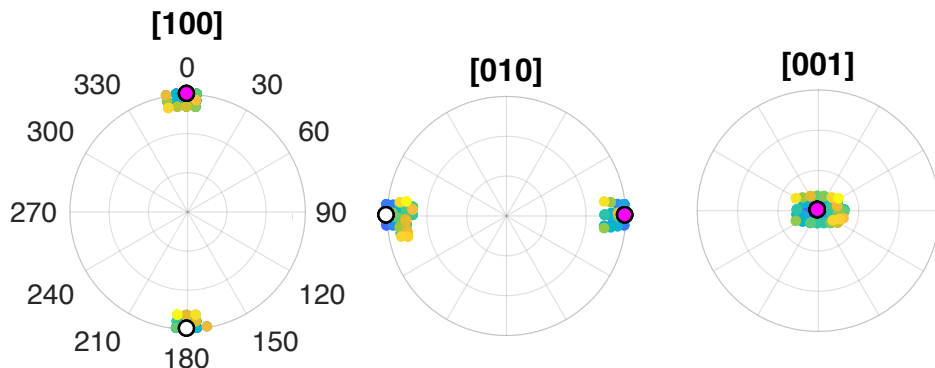


c) Calculate Fast Polarization Directions

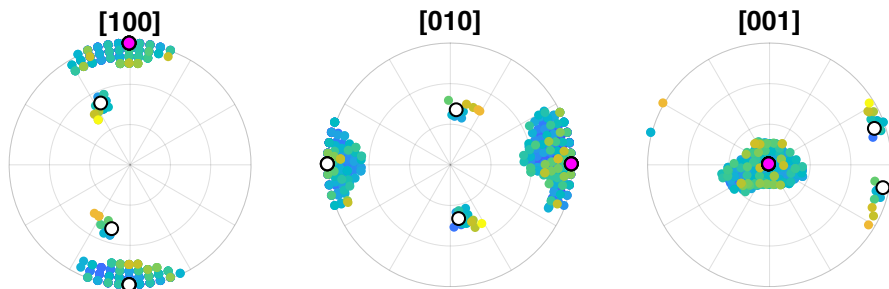




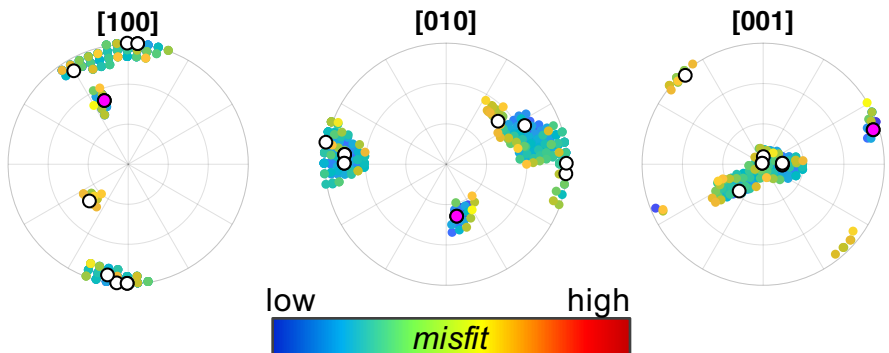
(a) 8 Measurements



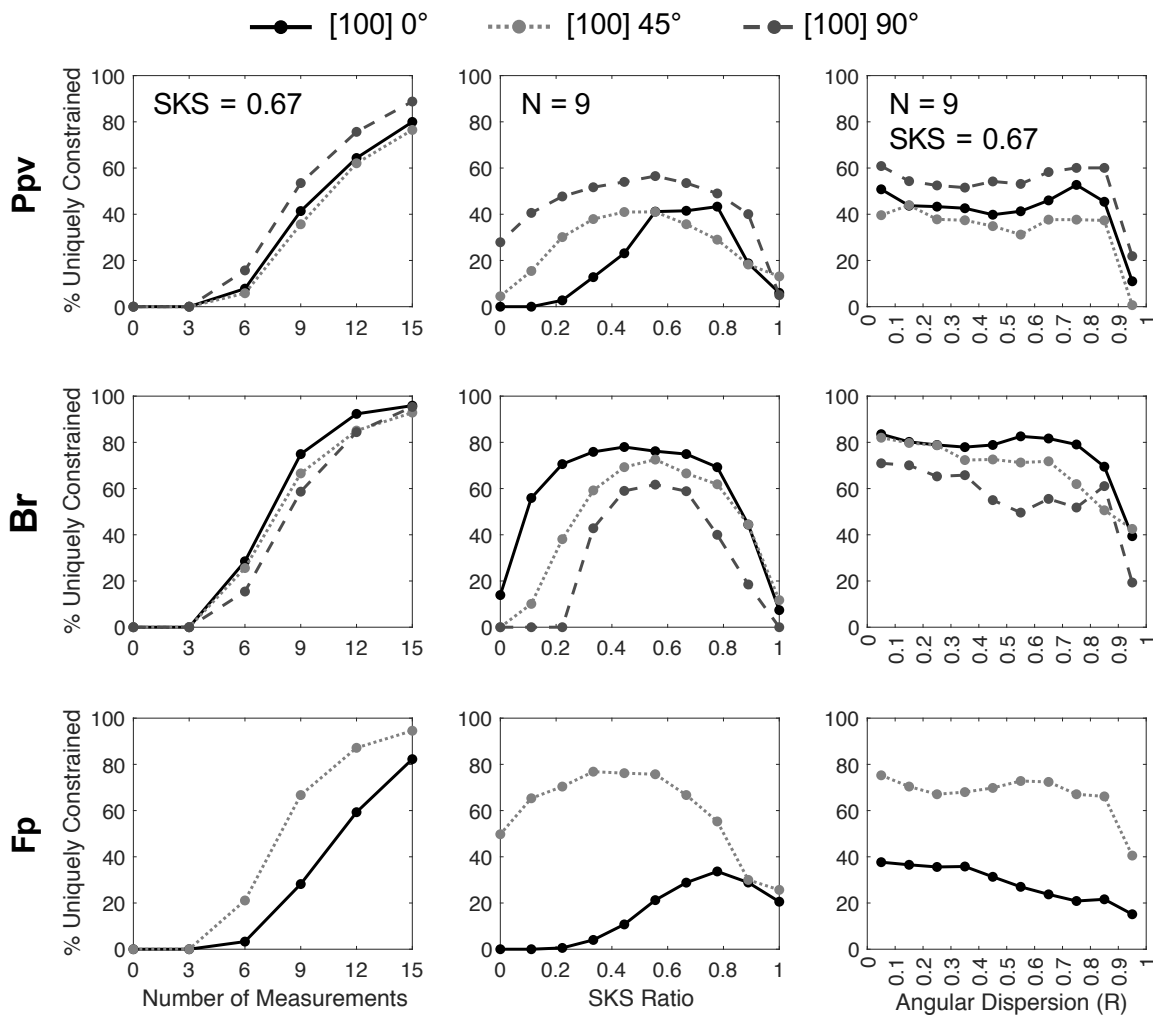
(b) 4 Measurements



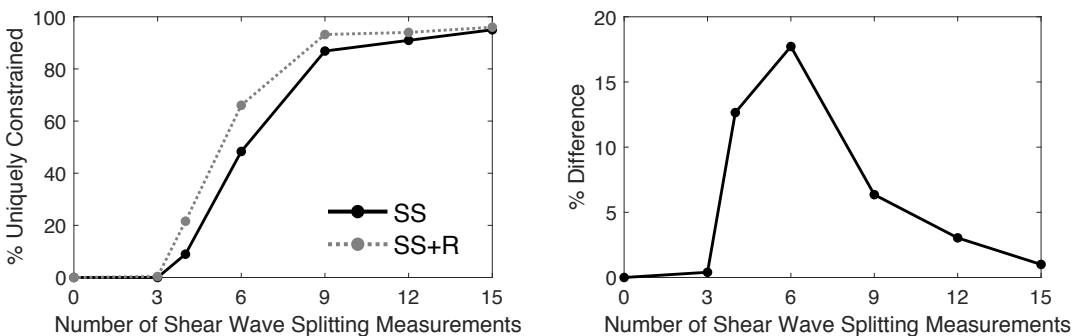
(c) 4 Measurements with Gaussian Error



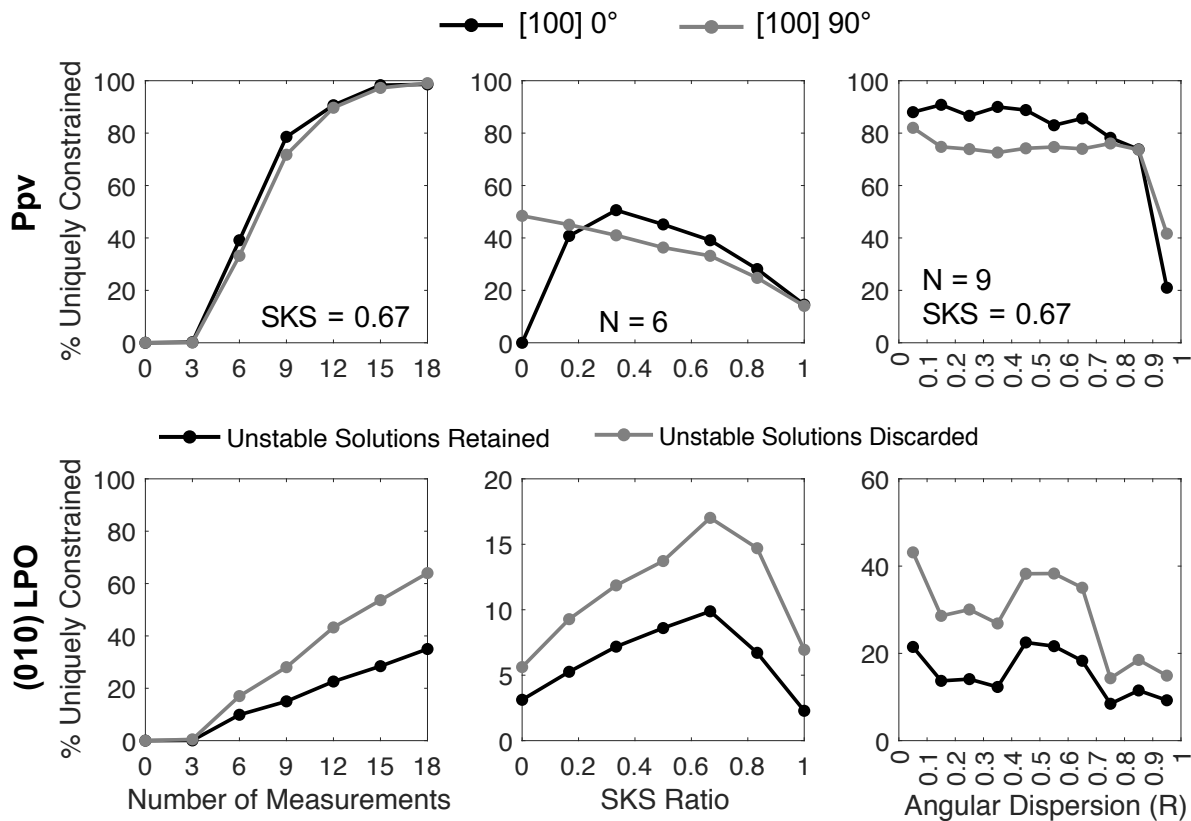
(a) Changes in the Starting Model



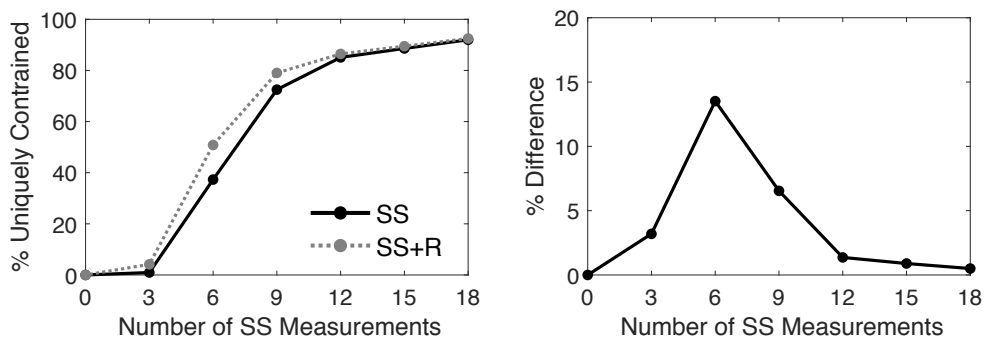
(b) Adding 1 Reflection Measurement

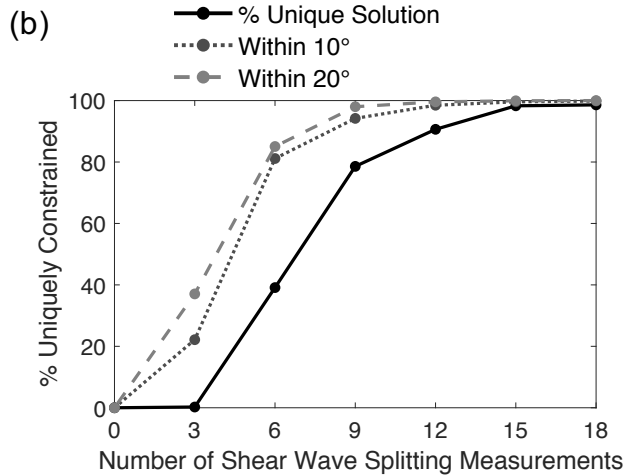
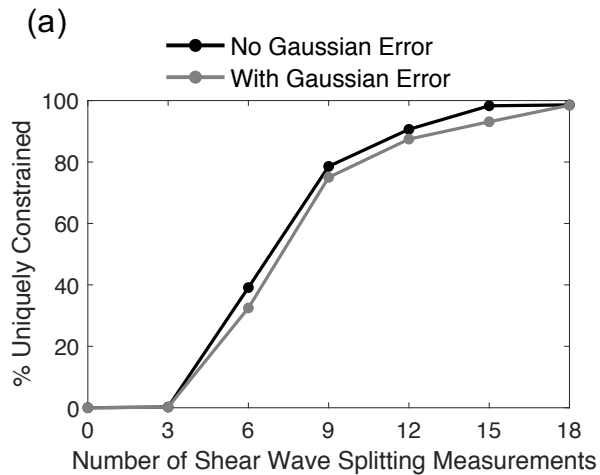


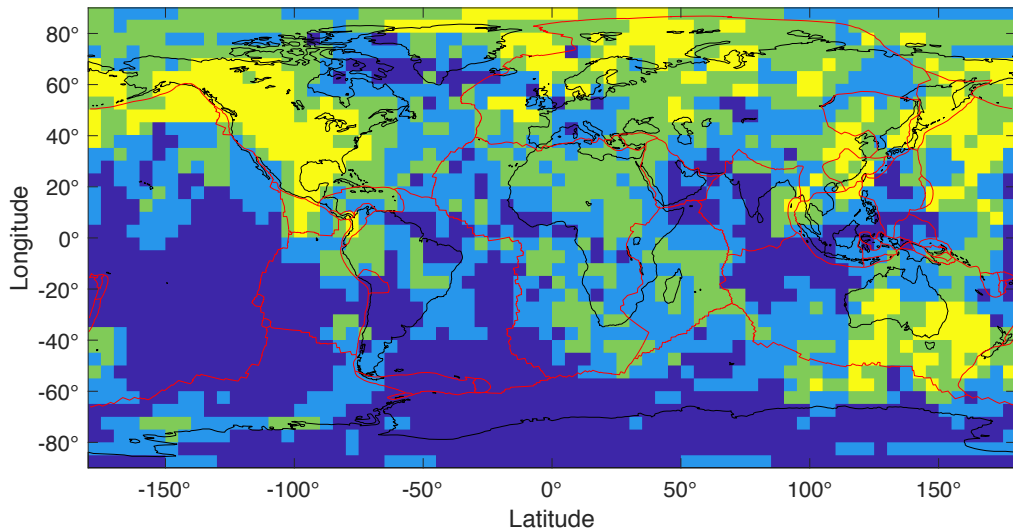
(a) Changes in the Starting Model Orientation



(b) Adding 1 Reflection Measurement







Supplemental Material:

Constraining lowermost mantle anisotropy with body waves: A synthetic modeling study

Neala Creasy^{1*}, Angelo Pisconti², Maureen D. Long¹, Christine Thomas², and James Wookey³

¹Department of Geology and Geophysics, Yale University

²Institut für Geophysik, Universität Münster

³Department of Earth Sciences, University of Bristol

*Corresponding author. Email: neala.creasy@yale.edu

Supplement Figures

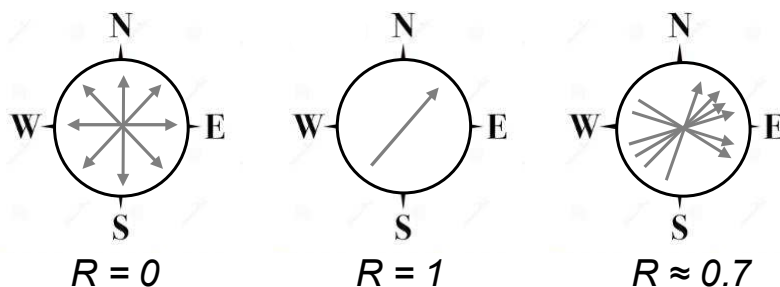


Figure S1. Schematic diagram showing the definition of angular dispersion (R), with arrows indicating a direction anywhere from 0° to 360° . Small values of R indicate a wide distribution of directions, while larger values indicate a tight configuration.

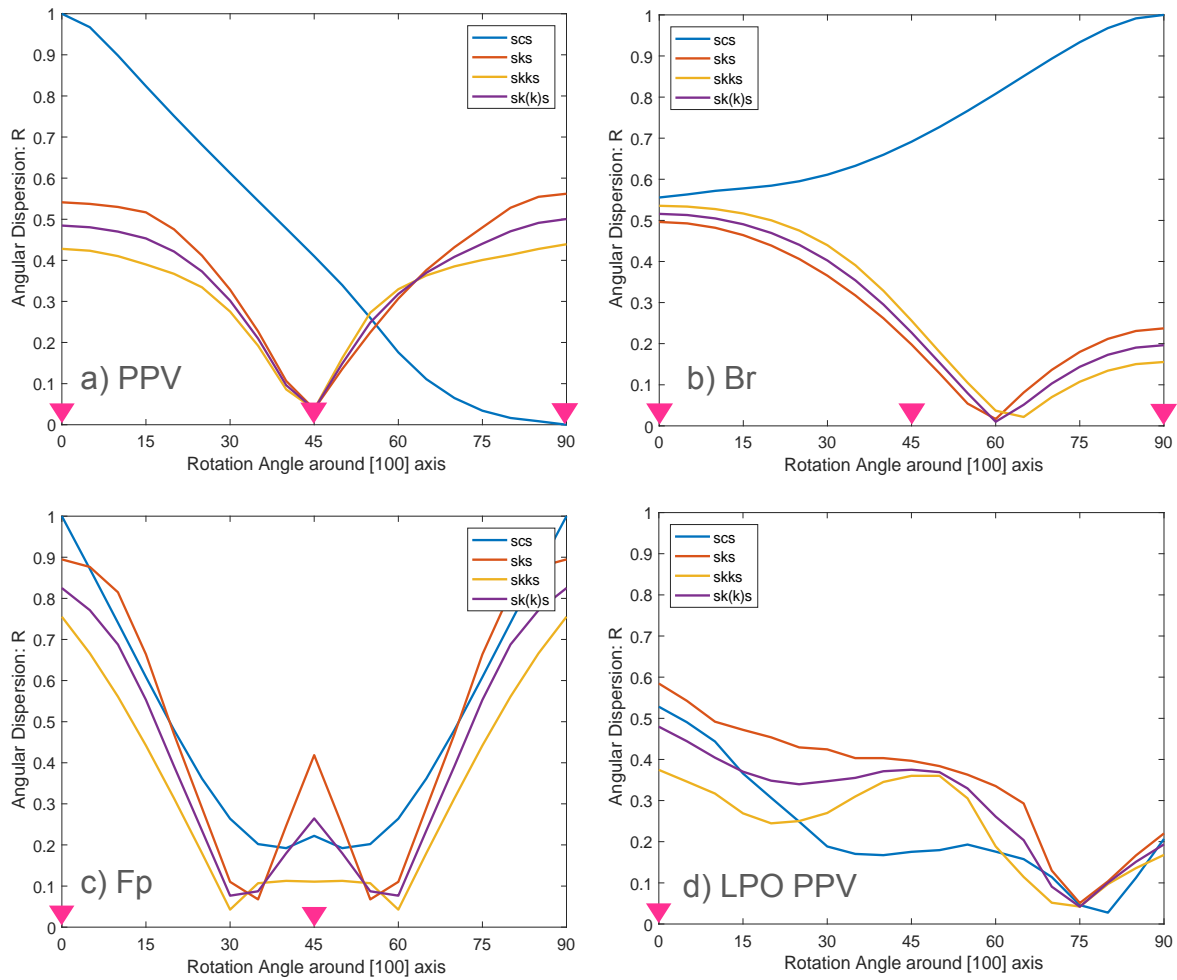
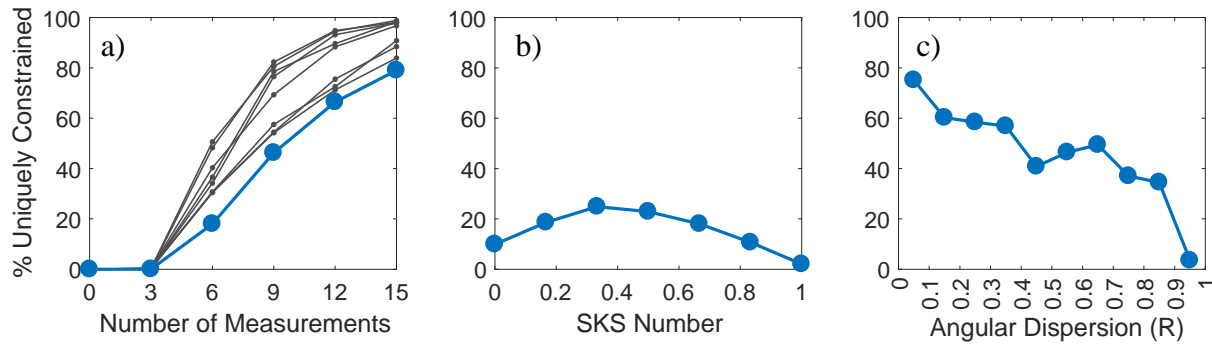


Figure S2. Angular dispersion – R – plots of all predicted fast axis directions for SKS (red), SKKS (orange), SKS and SKKS (violet), and ScS (blue). Equations (2) and (3) from the main text were used to calculate R; however, since fast axis directions can only vary from -90° to 90° , the fast axis orientations were adjusted from -90 to 90 to 0 to 360 . Angular dispersion is plotted in terms of the clockwise rotation angle about the [100] axis of (a) post-perovskite (PPV), (b) bridgmanite (Br), (c) ferropericlase (Fp), and (d) LPO of PPV of the given models, respectively. Magenta triangles indicate the starting models' orientations used in the modeling in the main text as in Figures 8 and 9.

31



32

33

34

35

36

37

38

39

40

41

42

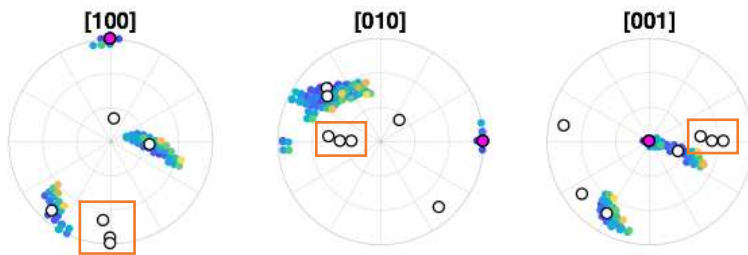
43

44

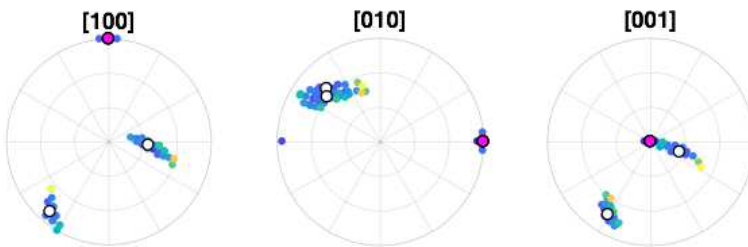
Figure S3. Results of synthetic tests that aim to uniquely constrain the orientation of a Ppv starting model, as discussed in section 3.3 in the main text, by selecting 9 random the starting orientations of the Ppv tensor. Each figure illustrates the probability of uniquely identifying the given starting model's orientation using the synthetic data, for nine different orientations of Ppv. As in Figure 7, each column represents the variable that was allowed to vary, while the other two were fixed. For (a), the SKS number was fixed (0.67). For (b), the number of measurements was fixed to six. For (c), the number of measurements was fixed to nine measurements and an SKS number of 0.67. The blue lines in (b) and (c) correlate to the blue line in (a), where the variation of SKS number and angular dispersion were only tested for one of the starting model orientations.



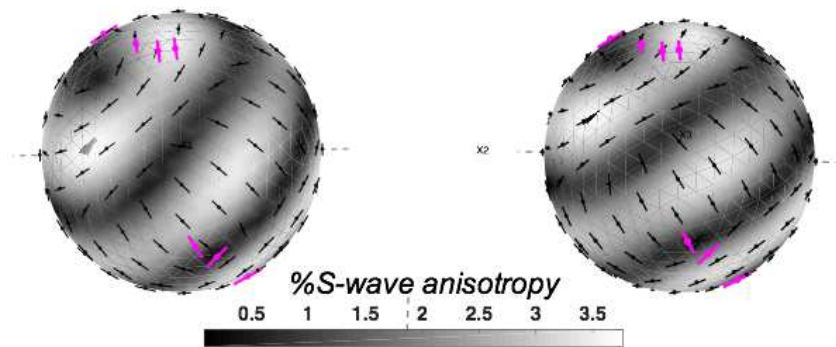
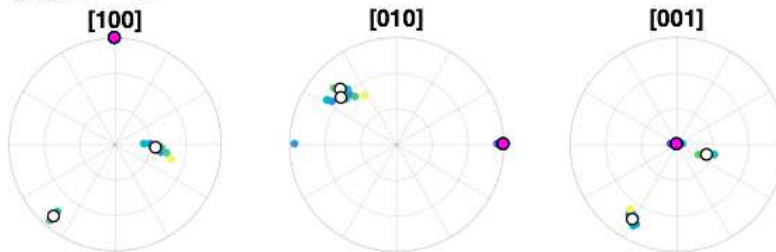
Cutoff = 20°



Cutoff = 15°



Cutoff = 10°



Unstable solution

Unstable solution rotated by 5
degrees, which fails the misfit
criterion

Figure S4: Example illustrating the identification of unstable solutions in a test that aimed to identify the starting orientation of a horizontal textured Ppv LPO. The polar plots show all possible orientations that fit a given synthetic dataset. The colors represent misfit values. The white circles mark the minimum misfit of each cluster of possible orientations. The magenta circles show the correct solution. The orange boxes highlight some of the unstable solutions. Each row represents a different misfit cutoff. The top row represents the cutoff used in this study (20°). The second row uses a cutoff of 15° and the third row 10° . With a lower cutoff, the unstable solutions are eliminated. The bottom elastic tensors on the left show an example of one of the resulting unstable solution from the orange boxes in the first row. The elastic tensor on the right shows the same tensor but rotated by 5° , which fails the misfit criterion. The magenta lines represent the measurements used in this simulation. Colors here represent %S wave anisotropy.